

DTIC FILE COPY

4

RADC-TR-88-27
Final Technical Report
February 1988

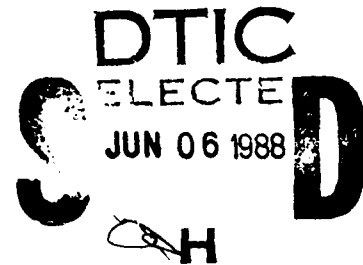


AD-A196 748

LEC GROWTH OF InP WITH MAGNETIC FIELD ASSISTED MELT STABILIZATION AND HEAT TRANSFER CONTROL

Massachusetts Institute of Technology

August F. Witt



APPROVED FOR PUBLIC RELEASE; DISTRIBUTION UNLIMITED

ROME AIR DEVELOPMENT CENTER
Air Force Systems Command
Griffiss Air Force Base, NY 13441-5700

UNCLASSIFIED
SECURITY CLASSIFICATION OF THIS PAGE

REPORT DOCUMENTATION PAGE				Form Approved OMB No 0704-0188	
1a. REPORT SECURITY CLASSIFICATION UNCLASSIFIED			1b. RESTRICTIVE MARKINGS N/A		
2a. SECURITY CLASSIFICATION AUTHORITY N/A		3. DISTRIBUTION / AVAILABILITY OF REPORT Approved for public release; distribution unlimited.			
2b. DECLASSIFICATION / DOWNGRADING SCHEDULE N/A		4. PERFORMING ORGANIZATION REPORT NUMBER(S) N/A			
4. PERFORMING ORGANIZATION REPORT NUMBER(S) N/A		5. MONITORING ORGANIZATION REPORT NUMBER(S) RADC-TR-88-27			
6a. NAME OF PERFORMING ORGANIZATION Massachusetts Institute of Technology		6b. OFFICE SYMBOL (if applicable)	7a. NAME OF MONITORING ORGANIZATION Rome Air Development Center (ESME)		
6c. ADDRESS (City, State, and ZIP Code) Dept of Materials Science & Engineering Cambridge, MA 02139			7b. ADDRESS (City, State, and ZIP Code) Hanscom AFB, MA 01731-5000		
8a. NAME OF FUNDING / SPONSORING ORGANIZATION Rome Air Development Center		8b. OFFICE SYMBOL (if applicable) ESME	9. PROCUREMENT INSTRUMENT IDENTIFICATION NUMBER F19628-84-K-0011		
8c. ADDRESS (City, State, and ZIP Code) Hanscom AFB, MA 01731-5000		10. SOURCE OF FUNDING NUMBERS			
		PROGRAM ELEMENT NO. 62702F	PROJECT NO. 4600	TASK NO. 17	WORK UNIT ACCESSION NO. 55
11. TITLE (Include Security Classification) LEC GROWTH OF InP WITH MAGNETIC FIELD ASSISTED MELT STABILIZATION AND HEAT TRANSFER CONTROL					
12. PERSONAL AUTHOR(S) August F. Witt					
13a. TYPE OF REPORT Final		13b. TIME COVERED FROM Jan 84 to Feb 87		14. DATE OF REPORT (Year, Month, Day) February 1988	15. PAGE COUNT 62
16. SUPPLEMENTARY NOTATION N/A					
17. COSATI CODES			18. SUBJECT TERMS (Continue on reverse if necessary and identify by block number)		
FIELD	GROUP	SUB-GROUP	crystal growth, InP, liquid encapsulated Czochralski, melt convection, segregation, melt stabilization, by magnetic fields, heat transfer control.		
20	02				
19. ABSTRACT (Continue on reverse if necessary and identify by block number) The research focuses on the optimization of InP growth by the LEC technique using magnetic fields for melt stabilization and heat pipes for the control of critical thermal fields. <i>InP growth</i>					
20. DISTRIBUTION / AVAILABILITY OF ABSTRACT <input checked="" type="checkbox"/> UNCLASSIFIED/UNLIMITED <input type="checkbox"/> SAME AS RPT. <input type="checkbox"/> DTIC USERS			21. ABSTRACT SECURITY CLASSIFICATION UNCLASSIFIED		
22a. NAME OF RESPONSIBLE INDIVIDUAL ALTON F. ARMINGTON			22b. TELEPHONE (Include Area Code) (617) 377-5017		22c. OFFICE SYMBOL RADC (ESME)

SUMMARY

The conducted research was directed at broadening the science base for LEC type melt growth of InP through the establishment of quantifiable thermal boundary conditions in the melt and through the stabilization of the melt by means of applied axial magnetic fields. In the extension, this research was aimed at systems development which have direct applicability in crystal growth technology.

In view of the non-availability of high temperature heat pipes throughout the duration of this research program, much of the work was carried out with analog model systems. This work yielded semiconductor single crystals in which all micro-segregation inhomogeneities - which characterize melt grown semiconductors - as well as radial macro-segregation effects were completely suppressed. Related modelling efforts revealed that pressure effects substantially influence the growth and segregation behavior as well as the generation and distribution density of dislocations during conventional, non-encapsulated growth. Pressures up to 35 atmospheres were not found to significantly influence segregation during LEC growth with B_2O_3 at layer thicknesses of 1 cm and more.

The fundamental concepts of this research effort were the basis for the most advanced research program on heat and mass transfer control with magnetic melt stabilization during low pressure LEC growth of GaAs sponsored jointly by DARPA/Air Force Materials Laboratory and for the extended research phase on "Development of Model Based Magnetic LP-LEC Growth: Large Diameter GaAs." Published results obtained in conjunction with this research have stimulated industrial development efforts in the area of high temperature heat pipes. Most recently Wah-Chang/Teledyne has announced the development of a prototype device which will be tested at MIT and applied to growth of GaAs and InP.

Accession For	
NTIS GRA&I	<input checked="" type="checkbox"/>
DTIC TAB	<input type="checkbox"/>
Unannounced	<input type="checkbox"/>
Justification	
By	
Distribution/	
Availability Codes	
Dist	Avail and/or Special
A-1	

I. Segregation in RF Heated High Pressure LEC growth

Continuing in an effort to elucidate the growth behavior during high pressure LEC growth of InP, a study of the segregation behavior was undertaken. This study's aim was to clarify differences, if any, between high pressure, RF heated Czochralski growth and conventional low pressure resistance heated growth of semiconductors in moderately dimensioned crucibles (6 cm diameter) with and without liquid encapsulation. The model system Ge:Ga was chosen for the following reasons:

- (1) quantitative segregation data is easily obtained from the elemental system Ge:Ga;
- (2) the melting point similarity between Ge and InP makes it an appropriate model for general segregation characteristics expected in the growth of InP;
- (3) the equilibrium segregation coefficient of Ga in Ge is comparable to Sn (a common dopant used in producing n type material) in InP.

This study was undertaken to investigate the difference, if any, between:

- (1) RF and resistance heating,
- (2) encapsulated vs. unencapsulated growth, as well as
- (3) low vs. high ambient pressure.

It was expected that axial micro-segregation in RF heated systems would be much more severe than that observed in resistance heated growth due to the unavoidable problem of alignment of the susceptor within the RF coil and the differential coupling that would be experienced. This effect was expected to lead to pronounced thermal asymmetry in the growth environment.

Experimental Results

A series of Ge:Ga crystals were grown from quartz crucibles under conditions in which most of the critical growth parameters were systematically varied. Subsequent to growth, crystal sections containing the rotational axis of the growing crystal were cut with a diamond saw. These samples were subsequently (1) mounted on brass disks with In:Sn solder to form back side ohmic contacts, (2) lapped with 5 μm Al_2O_3 , and (3) polished with a solution of 200 ml Nalcoag 2355 colloidal silica, 400 ml DI water, and 6 ml H_2O_2 .

After achieving a mirror finish on the sample surface, the crystals were etched in a solution of $\text{HF}:\text{CH}_3\text{COOH}:\text{H}_2\text{O}_2$ (1:1:1) to reveal compositional variations (growth striations). These samples were then subjected to single point spreading resistance

measurements to obtain quantitative data related to the segregation behavior of Ga in the Ge. Focus was placed upon:

- (1) axial macro-segregation: the determination of the effective segregation coefficient;
- (2) axial micro-segregation;
- (3) radial macro-segregation to obtain information related to the shape of the solute boundary layer, as well as information related to bulk melt flows.

The matrix of growth experiments undertaken is listed in table 1.

Results and Discussion

The Effect of Pressure and Encapsulation on Segregation

Crystals were grown to investigate the effects of pressure and encapsulation upon segregation in the standard high pressure growth environment. Typical micro-segregation data from these crystals is presented in fig. 1. (Note that the non-encapsulated crystal turned polycrystalline immediately upon a pressure change; hence, there is no data for this portion of the crystal.) The charge carrier profile is essentially flat, showing a lack of any evidence of rotational striations. Previously, it was reported that encapsulation in small scale systems had the effect of eliminating micro-segregational inhomogeneities by creating a transition from turbulent melt convection to laminar forced convection through the establishment of (a) a reduced destabilizing thermal gradient and (b) retarding the convective melt flows through the establishment of a shear boundary layer at the melt/encapsulant interface. In the present study on growth with larger crucible sizes, it is seen that the encapsulant does not bring about these transitions, as indicated by the turbulence dominated micro-segregation profile. This can be understood through consideration of the increased Reynolds number with increasing dimensions, and hence a larger driving force for turbulent thermal natural convection. The radial segregation data exhibit a flat profile, indicative of either a highly uniform or virtually non-existent solute boundary layer, consistent with a highly turbulent melt.

The axial macro-segregation data allowed for the calculation of k_{eff} based upon the Scheil equation:

$$\frac{C_s(g)}{C_l(g)} = k (1 - g)^{k-1}$$

From axial macro-segregation data, the effective segregation coefficient for the high and low pressure regions of sample 1 were calculated. These values were found to be:

low pressure (50 psi): $k_{eff} = 0.62$

high pressure (100 psi): $k_{eff} = 0.60$

Considering the error limits in the measurement technique, it can be stated that the two values are the same; hence the change in pressure had no apparent effect on the macroscopic segregation behavior. It is noted though, that these values are extremely high for the Ge:Ga system ($k_0 = 0.087$). An analysis of the boundary layer thickness for this experimental finding (k_{eff}) according to the BPS theory yields:

$$\delta = \left[\frac{D}{R} \right] \left\{ \ln \left(\frac{1}{k_0} \right) - \ln \left(\frac{1}{C_s / C_1} - 1 \right) \right\}$$

$R = \text{growth rate} = 1.11 \times 10^{-3} \text{ cm/s}$

$D = 1.9 \times 10^{-4} \text{ cm}^2 / \text{s}$

$k_0 = 0.087$

$C_s / C_1 = 0.6$

$\delta = 0.41 \text{ cm}$

When comparing this δ value, complications in the data interpretation become evident with that obtained through a Cochran analysis for a rotating disk:

$$\delta = 1.6 D^{1/3} \nu^{1/6} \omega^{-1/2}$$

where:

$D = 1.9 \times 10^{-4} \text{ cm}^2 / \text{s}$

$\nu = 1.4 \times 10^{-3} \text{ cm}^2 / \text{s}$

$\omega = \text{rotation rate}$

$\delta = 5.2 \times 10^{-3} \text{ cm}$

It is observed that the BPS analysis gives a boundary layer thickness which is in total contradiction with the establishment of convective melt flows. It is also noted that for much of the growth, the boundary layer thickness as predicted by BPS is found to be greater than depth of the melt.

Resistance vs. RF Heated Growth

To clarify the anomalously high k_{eff} as well as the reasons for the lack of rotational striations (periodic compositional variations), several crystals were grown. The axial micro-segregation data from a crystal grown in an LP-Resistance heated furnace (fig. 2) shows periodic compositional fluctuation which correlated with the seed rotation rate. There is no evidence of non-rotational compositional variations. This lack of turbulent convection in the case of resistance heated growth can be explained by considering the fundamental differences between the heat transfer in the two modes of heating (fig. 3). In the case of RF growth (with a conventional susceptor configuration) a large driving force for convection is expected due to the general bottom heating nature of the thermal configuration.

Radial etch and charge carrier profiles (fig. 4) are seen to exhibit an essentially flat growth morphology consistent with a uniform solute boundary layer. Axial macro-segregation data again suggest a k_{eff} of approximately 0.6 (figs. 5 & 6).

Anomalous Axial Macro-Segregation

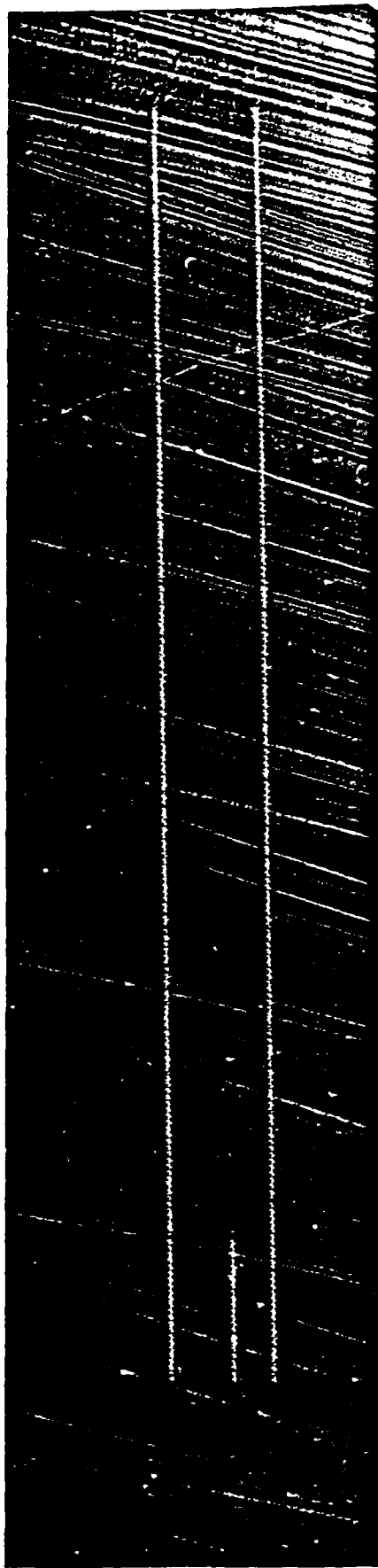
In response to the anomalously high k_{eff} found under all growth conditions, a series of crystals were examined to clarify this effect. Related representative axial macro-segregation data is presented in figures 7 - 11. In fig. 7 the Scheil equation's graphical analysis is shown. It is seen that this analysis leads to a k_{eff} of 0.519. In figures 8 and 9, the concentration data is plotted along with the theoretical concentration profiles for k_{eff} equal to 0.1 and 0.519 respectively. These graphs show that the concentration data follow a k_{eff} of ~ 0.1 up to $g = 0.5$, while following a k_{eff} of ~ 0.5 for the second half. Figures 10 and 11 show raw data; in this case, the effective segregation coefficient is in the range expected for conventional C_z growth. This inconsistent behavior indicates that a condition of uncontrolled bulk flow is affecting the segregation behavior in a manner which makes reproducible growth and hence comparison of data impossible.

Conclusions

1. The heat transfer differences between conventional RF heating and resistance heating gives rise to a large driving force for turbulent convection in RF heated growth.
2. Encapsulation does not bring about a transition from turbulent to laminar flow in a growth system of moderate dimensions.
3. Pressure has no detectable effect upon the macro and micro segregation characteristics.

Table 1

Sample	Furnace Type	Encapsulant	SRR	PR	Pressure
1	HP-RF	No	15	4 cm/hr	50/100 psi
2	HP-RF	Yes (1 cm)	15	4	50/100 psi
3	HP-RF	Yes (1 cm)	4	4	300/500 psi
4	LP-Res.	No	15	4	1 atm
5	LP-Res	No	15	4	1 atm
6	HP-RF	No	15	4	100 psi
7	LP-RF	No	15	4	1 atm
8	LP-RF	No	15	4	1 atm



10¹⁹

CARRIER CONCENTRATION



E14-1.CON

DISTANCE (MICRONS)

Fig. 1.1

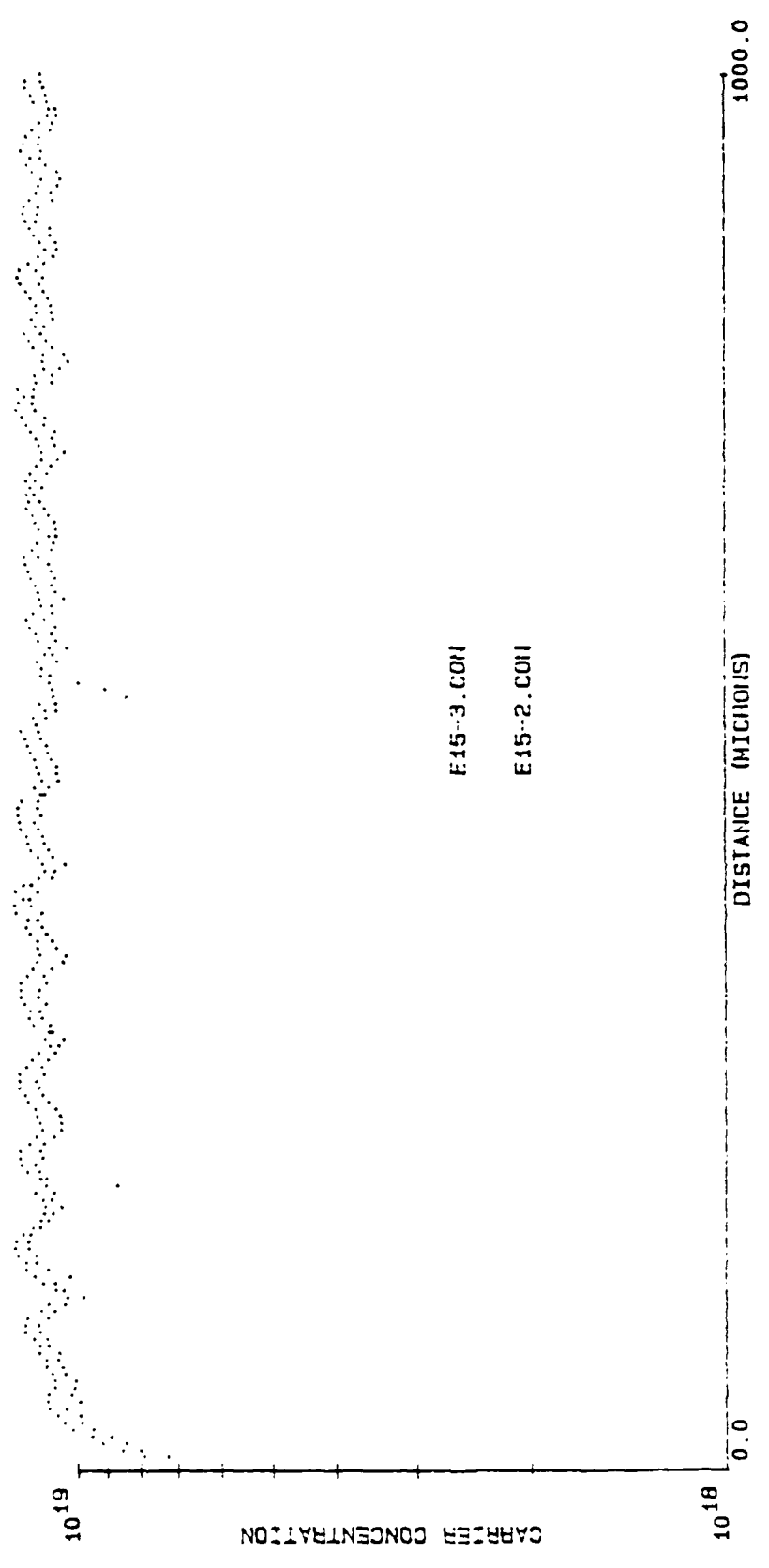
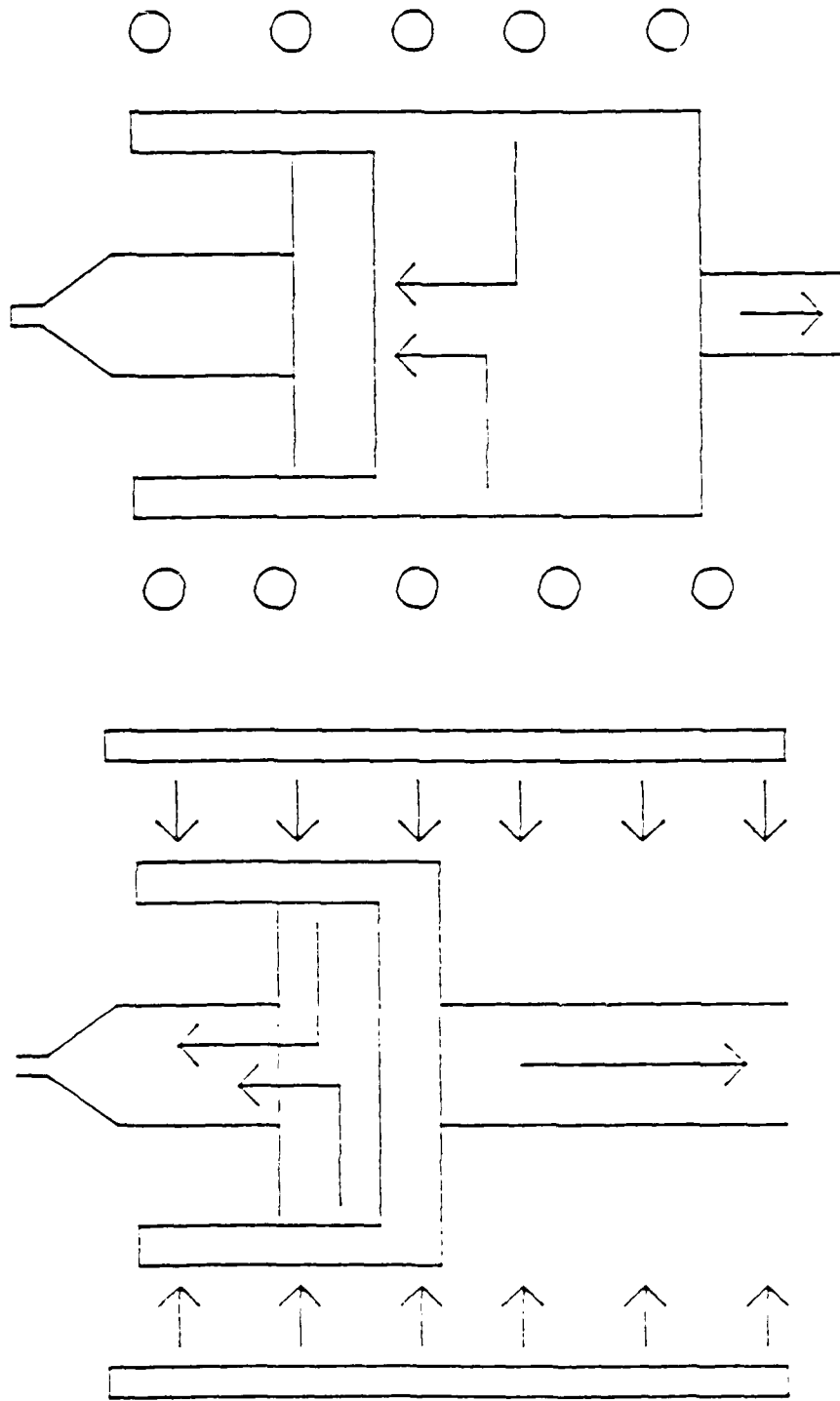


Fig. 1.2



Conventional RF Heating

Conventional Resistance Heating

Fig. 1.3

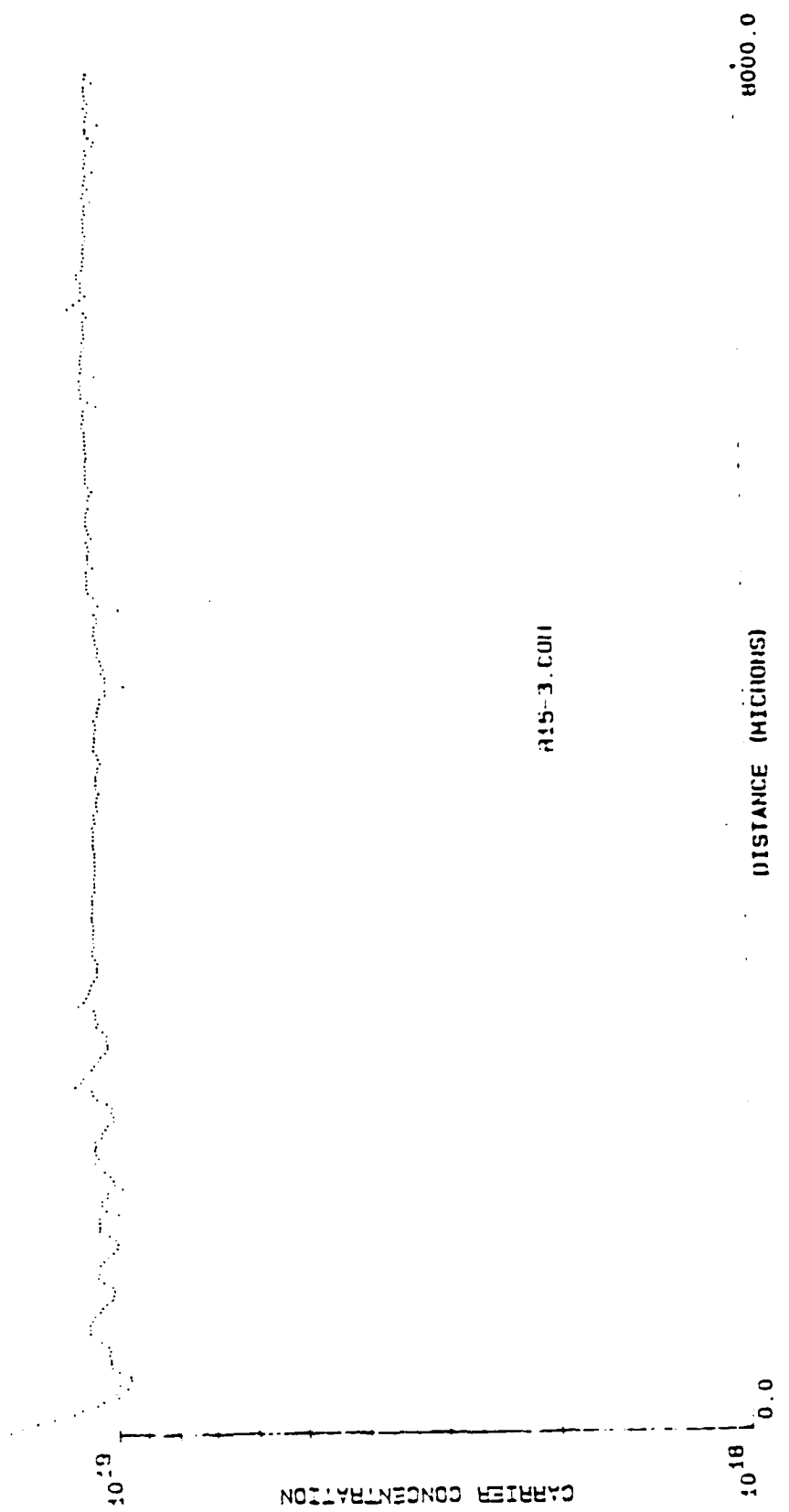


Fig. 1.4

GeGA15

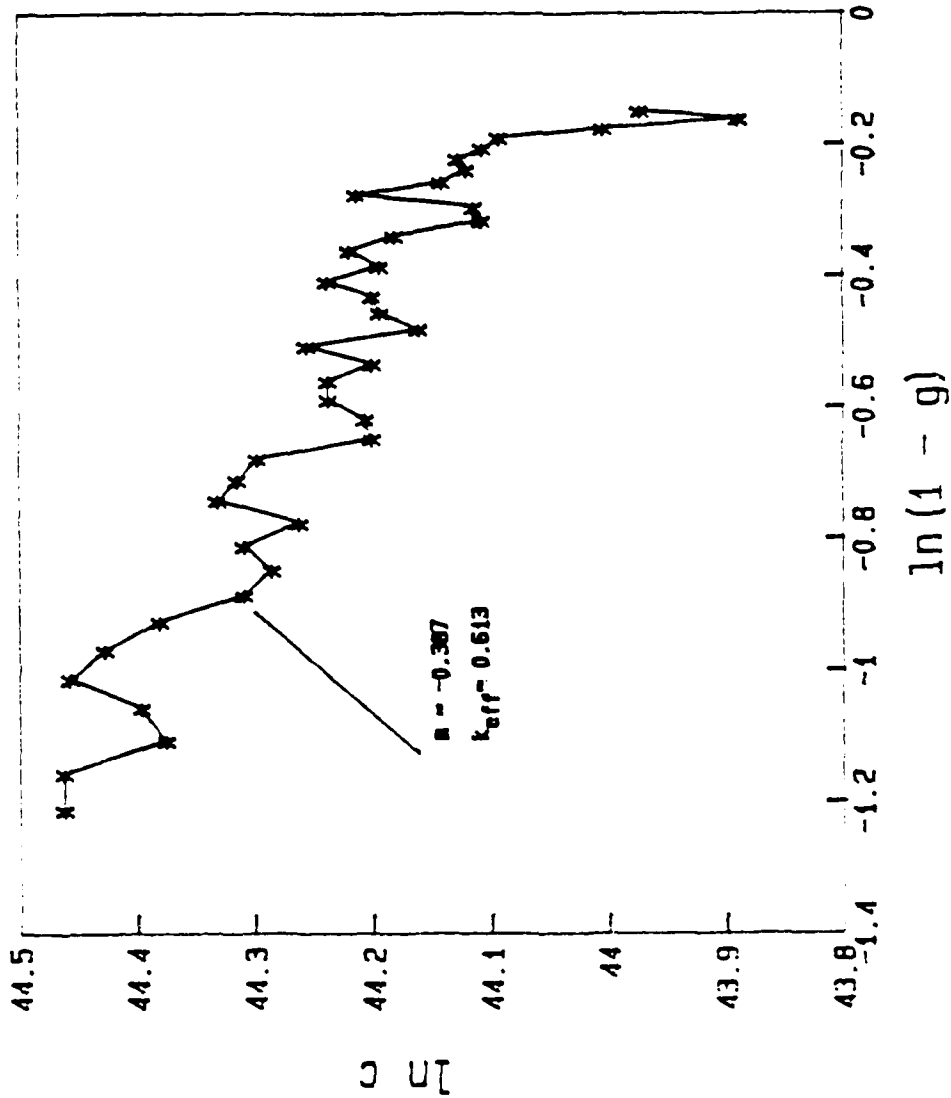


Fig. 1.5

GeGa15

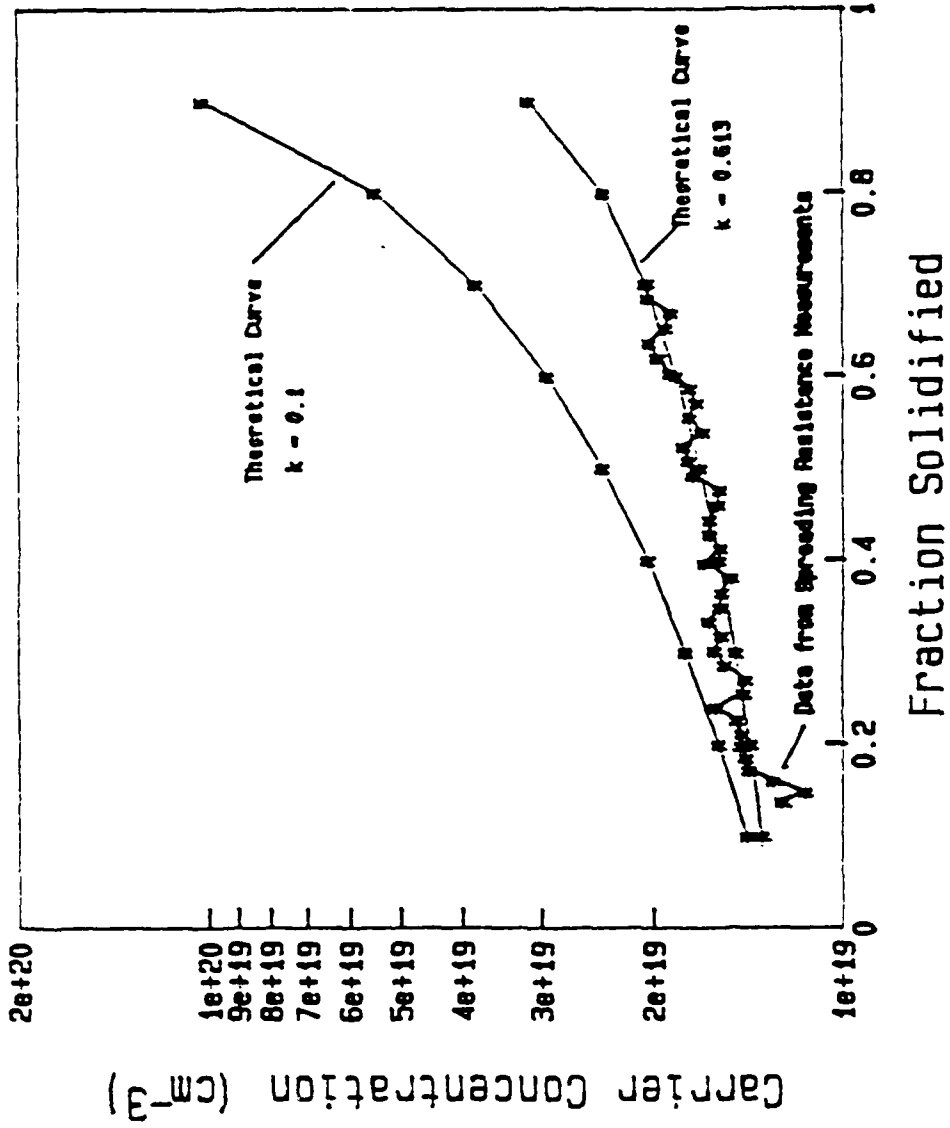


Fig. 1.6

GeGa18
Grown in RF Heated Furnace

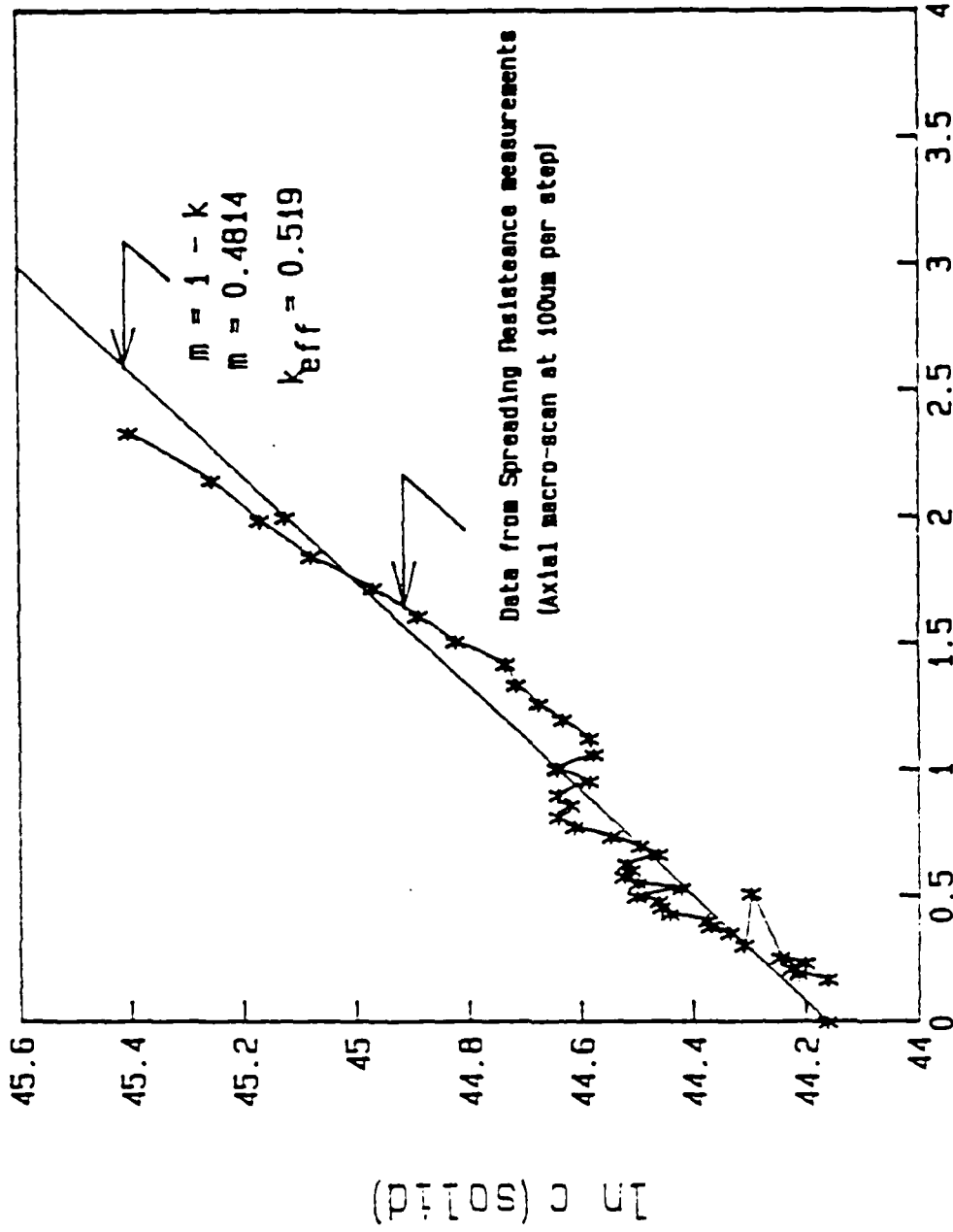
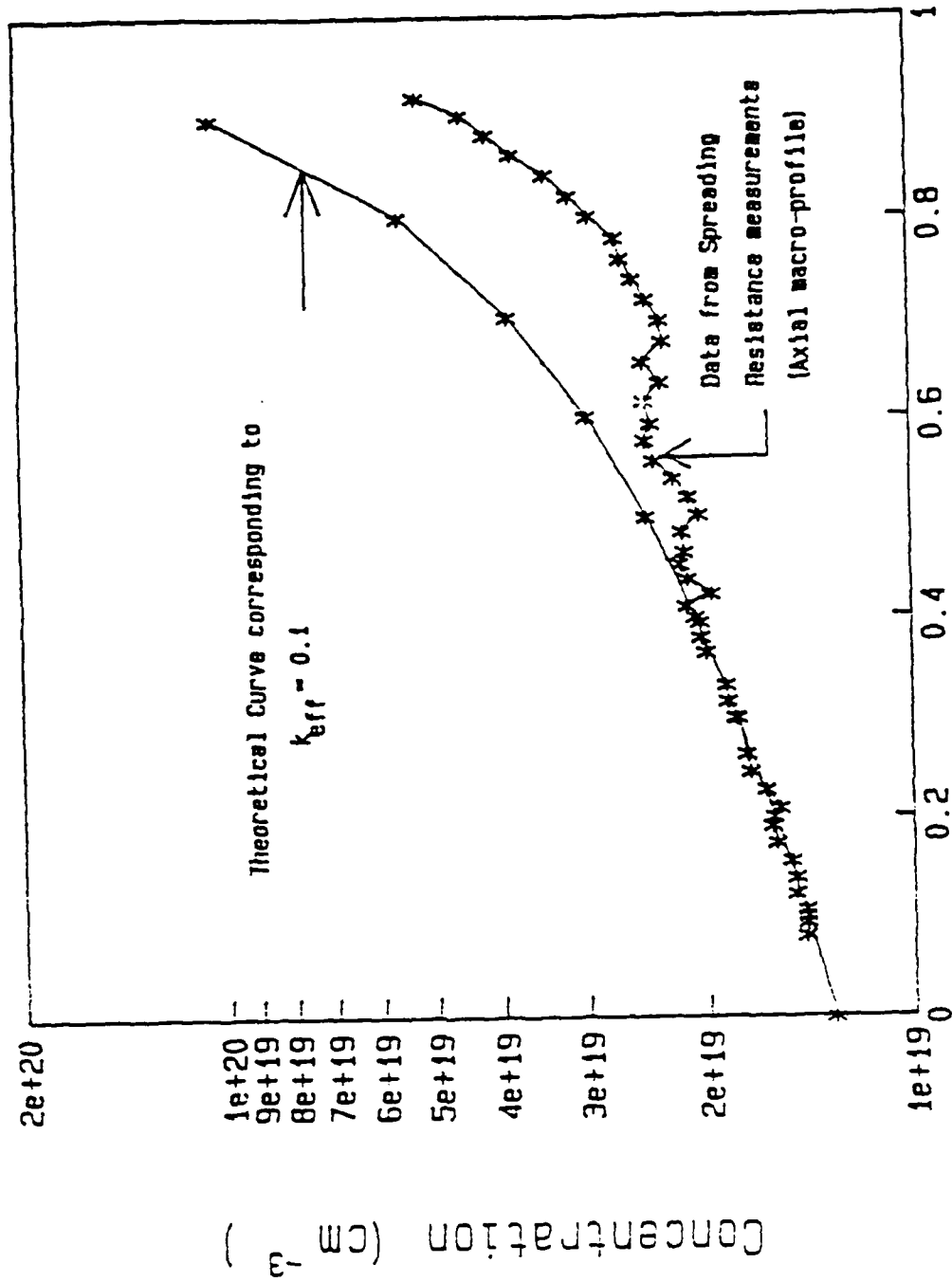


Fig. 1.7

GeGa18



Fraction Solidified (g)

Fig. 1.8

GeGa18

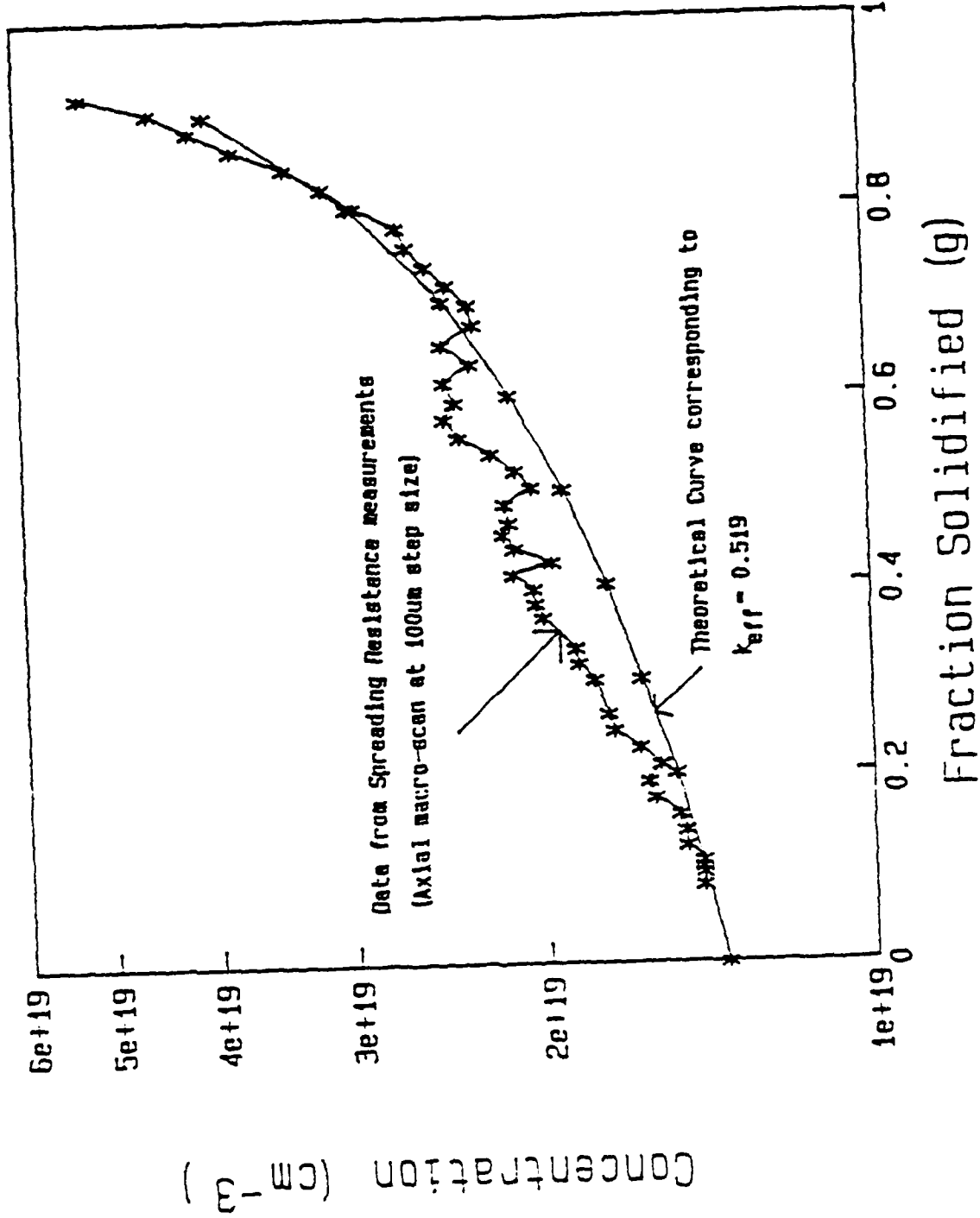
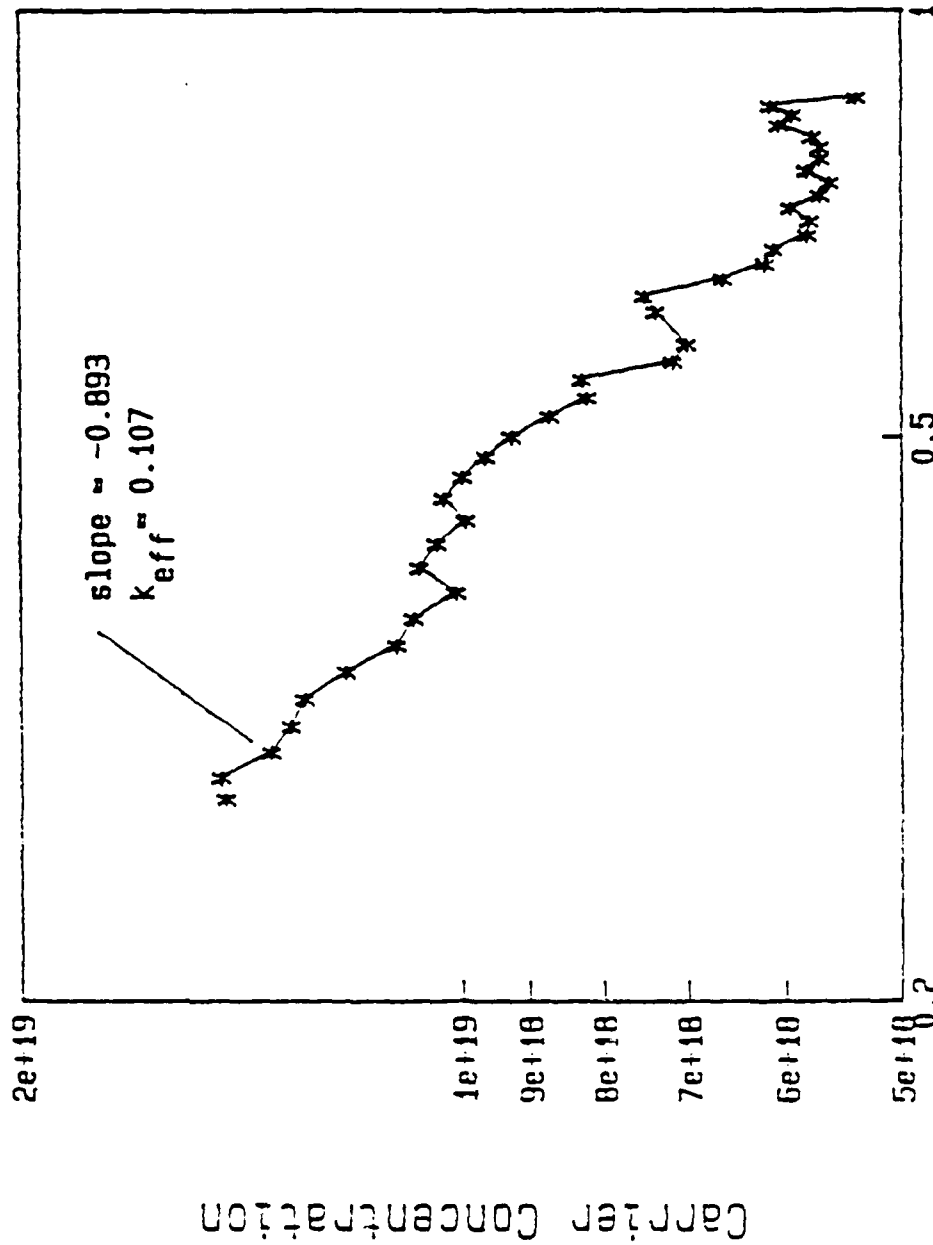


Fig. 1.9

GeGa19



1 - 9

Fig. 1.10

GeGa19

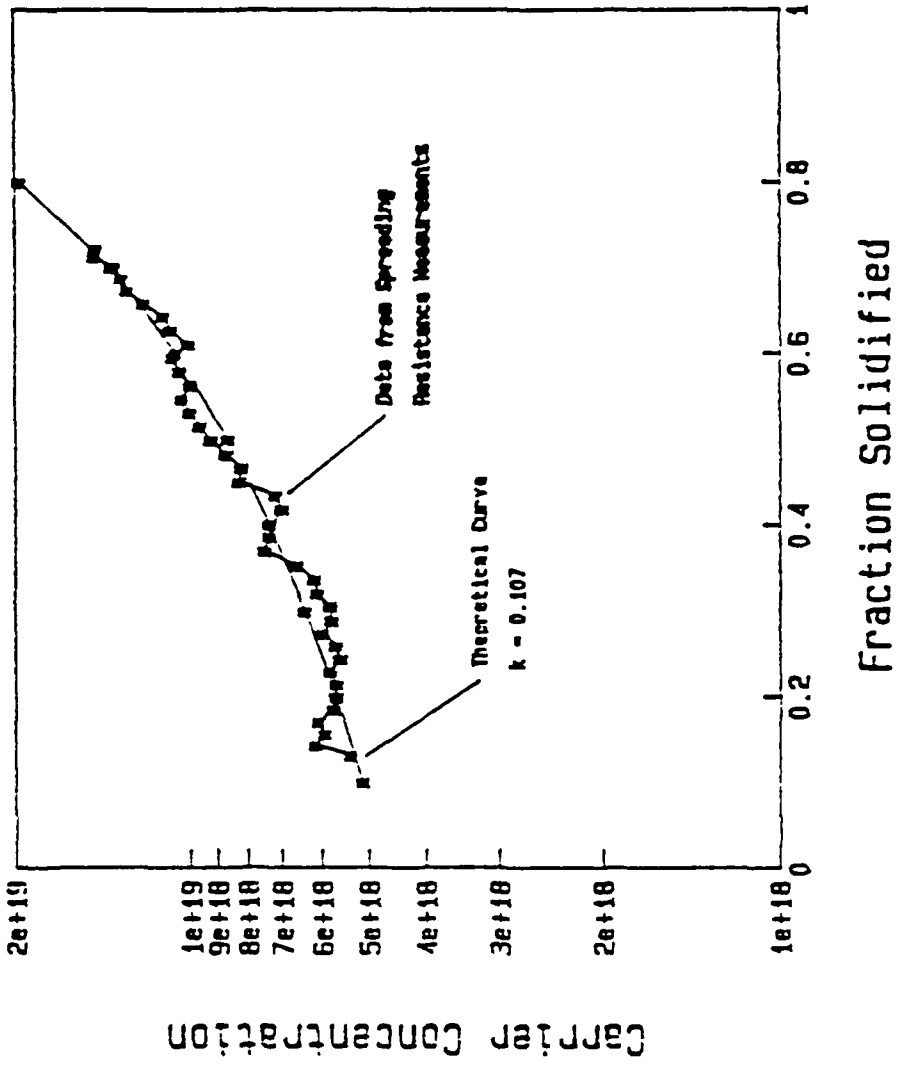


Fig. I.11

II. Heat Transfer in High Pressure Growth of InP

Analytical calculations of the relative contributions of radiational and convective heat transfer from the surface of an InP crystal grown at ambient pressures from 0–40 atm. are presented. These calculations were then used as a guide to the modification of a finite element heat transfer model of LEC GaAs growth for InP growth.

Excess thermal stress has been considered to be one of the major causes for dislocation generation in III–V compound semiconductors [1–3]. In thermal stress/heat transfer models of LEC growth, focus is on GaAs. These analyses are often adapted to InP, but the effect of the high pressure ambient gas is neglected in heat transfer calculations. For this reason, the convective contribution to heat transfer relative to radiational heat transfer has been analytically calculated. These calculations were then used as a guide in the modification of the model of Motakef [3] to take into consideration the physical properties of InP as well as the inclusion of geometric and convective heat transfer considerations specific to the growth of InP.

Radiation vs. Convection: The Effect of the Ambient Pressure

To evaluate the relative contributions of radiation and convection to heat transfer as a function of pressure, the non-dimensionalized heat flux from the crystal surface for each effect was calculated. The radiational flux is formulated as:

$$q''_R = \epsilon \sigma F (T_1^4 - T_2^4)$$

$$\overline{q''}_R = R_n (\Theta_1^4 - \Theta_2^4)$$

where:

$$\Theta = \frac{T}{T_m}$$

$$R_n = \text{radiation number}$$

$$= \frac{\epsilon \sigma F T_i^4 r_c}{k_c}$$

The non-dimensional convective heat flux is expressed as:

$$q''_c = h (T_1 - T_2)$$

$$\overline{q''_c} = Bi (\Theta_1 - \Theta_2)$$

where:

$$Bi = \frac{h r_c}{k_c}$$

where :

$$h = 0.525 Ra^{1/4} \left\{ \frac{k}{D} \right\}$$

$$= 0.525 (Pr Gr)^{1/4} (k/D)$$

Using the above equations, the relative contributions to heat transfer were calculated for ambient pressures between 1 and 40 atmospheres and temperature differences (between the crystal surface and the ambient) of 400 and 600 degrees. Table 1 shows the calculated contributions which are presented graphically in fig. 1 as $(\overline{q}_{conv} / \overline{q}_{rad})$ vs. pressure. It is seen that at the pressures used for the LEC growth of InP ($P > 27.5$ atm), convective heat transfer contributes more than 1/4 to the possible heat transfer in the system. This graph suggests that the effects of convective heat transfer are negligible in modelling the growth of low pressure systems, but convective heat transfer must be considered in high pressure systems.

Finite Element Modelling

Constant crystal diameter, absence of crystal shoulder

As the first attempt in modelling, the finite element code of Motakef [3] was modified to account for the thermo-physical properties of InP (table 2) and to allow for convective heat transfer boundary conditions. In this model a cylindrical crystal was assumed to grow from a melt encapsulated with an optically transparent encapsulant. Two cases were studied: one without and one with convective heat transfer boundary conditions at the crystal/gas interface as well as at the encapsulant/gas interface. Figures 2 and 3 show the excess thermal stress profiles at the crystal center, half radius and the periphery as a function of non-dimensional axial location. From these two plots it is clear that convection in the gas phase alters both the positions and the magnitude of the maximum excess stress. The stress level in the crystal was found to increase by about 25% in a high pressure environment. This indicates that any heat transfer control approach in the growth of InP must address convection in the gas phase.

Crystal with conventional shoulder and a transparent or opaque encapsulant

Since a cylinder does not closely model the actual shape of Czochralski grown InP, it was decided to evaluate the effect of shoulder geometry upon the temperature distribution in the crystal. In this case it is important to consider that non-linearities in the temperature field give rise to thermal stress. Figure 4 presents the calculated temperature field for an InP crystal with a 60° shoulder encapsulated by a transparent encapsulant. The isotherm profile exhibits pronounced curvature in the shoulder region; this finding can be interpreted as:

1. The shoulder acts as a funnel through which the heat must move creating a restriction to heat flow and hence extreme curvature in the isotherm profile;
2. The shoulder surface radiates heat to the cold upper furnace wall, thus drastically increasing the heat transfer from this surface.

In the case of an opaque encapsulant, an inflection in the isotherm curvature can be noted (fig. 5). The magnitude of curvature is less than for the transparent encapsulant which suggests that a thermally opaque encapsulant may be more favorable for thermal stress reduction than the semi-transparent B_2O_3 used extensively. It must, however, also be considered that a thermally opaque encapsulant will, through its isolating effect, substantially reduce radial thermal gradients in the melt and thus impede diameter control during growth.

Shoulder and opaque encapsulant at two stages during growth

Since the dislocation generation and density distribution will be affected by all of the stress distributions that the crystal experiences during growth, two different stages of growth were modeled, both while the crystal was still being greatly affected by the shoulder region. In the first case (fig. 6) the crystal is fully immersed in an opaque encapsulant. As seen in fig. 7, the stress distribution, already at this early stage of growth, greatly exceeds CRSS. The stress distributions at varying axial locations (figs. 8-12) show the existence of the now classical "W" shaped radial profile. At most locations away from the crystal/melt interface the excess stress profile is found to be relatively low and flat.

A later stage in growth (after the shoulder has emerged from the encapsulant but the crystal has not been rounded to constant diameter) is depicted in fig. 13. In this case, we see that the crystal experiences two maxima in its stress profile (fig. 14), one at the crystal/melt interface and one at the encapsulant/gas interface. Examining the radial profiles of the stress distribution, a much more pronounced "W" shape in the stress distribution as compared to earlier stages of growth is observed. As with the earlier case (figs. 15-21), the level of stress decreases and the degree of variation decreases in the axial direction above the encapsulant. This is in

qualitative agreement with the dislocation density distribution (both radial and axial) observed on InP crystals grown in this laboratory.

Conclusions

1. The high pressure ambient gas has a significant effect on the heat loss from the crystal surface, contributing as much as 35% to the overall heat transfer.
2. The geometry of the crystal (the shoulder) serves to increase the lack of planarity in the temperature profile in the crystal, giving rise to larger thermal stresses.
3. Even during the earliest stages of growth, when the crystal shoulder is still fully in the encapsulant, the matrix experiences severe excess stress, suggesting that in the case of InP fully encapsulated growth likely may not be effective in reducing the dislocation density in InP.

References

1. A.S. Jordan, R. Caruso, and A.R. von Neida, The Bell Syst. Tech. J. **59** (4) 593 (1980).
2. A.S. Jordan, J. Crystal Growth, **71**, 559 (1985).
3. S. Motakef and A.F. Witt, J. Crystal Growth **80** (1) 37 (1987).

Table 1

$\Delta T = 400$							
P	Gr	Ra	Nu	h	Bi	qc	qc/qr
1	2.02e5	1.35e5	10.06	8.85	.00974	.00292	.0506
5	5.05e6	3.37e6	22.49	19.79	.0218	.00645	.113
10	2.02e7	1.35e7	31.82	28.00	.0308	.00924	.160
15	4.55e7	3.03e7	38.95	34.28	.0377	.0113	.196
20	8.08e7	5.39e7	44.98	39.58	.0435	.0131	.227
25	1.26e8	8.41e7	50.28	44.25	.0487	.0146	.253
30	1.82e8	1.21e8	55.06	48.45	.0533	.0160	.277
35	2.48e8	1.65e8	59.50	52.36	.0576	.0173	.3
40	3.23e8	2.15e8	63.61	55.98	.0616	.0185	.32
$\Delta T = 600$							
1	1.35e5	8.91e4	9.07	7.98	.009	.00401	.058
5	3.38e6	2.23e6	20.29	17.86	.0196	.0088	.128
10	1.35e7	9.0e6	28.76	25.31	.0278	.0125	.182
15	3.04e7	2.03e7	35.24	31.01	.0341	.0153	.222
20	5.40e7	3.60e7	40.66	35.78	.0393	.0177	.257
25	8.44e7	5.63e7	45.47	40.01	.0440	.0198	.288
30	1.22e8	8.14e7	49.87	43.89	.0483	.0217	.315
35	1.65e8	1.10e8	53.77	47.32	.0521	.0234	.340
40	2.16e8	1.44e8	57.51	50.61	.0557	.0237	.344

Table 2

Thermoelastic and Growth Properties of InP

InP

Thermal Conductivity (W/cm K)	$1215 T^{-1.324}$
Surface emissivity	0.5
CRSS (dynes/cm K)	$10(1.24 + 58.05/T)$
Young's Modulus	9.51×10^{11}
Poisson's Ratio	0.287
Elasticity	7.5×10^{-6}

Encapsulant (Boric Oxide)

Thermal Conductivity (W/cm K)	$2.37 \times 10^{-3} + 1.1 \times 10^{-5} T$
-------------------------------	--

Growth System

Ambient Gas: Argon

Temperature:	700 K
Viscosity	5.72×10^{-4}
Thermal conductivity	0.044

Furnace Wall Temperature: 400 K

Encapsulant Radiation Number 3.29

Crystal Radiation Number 0.0758

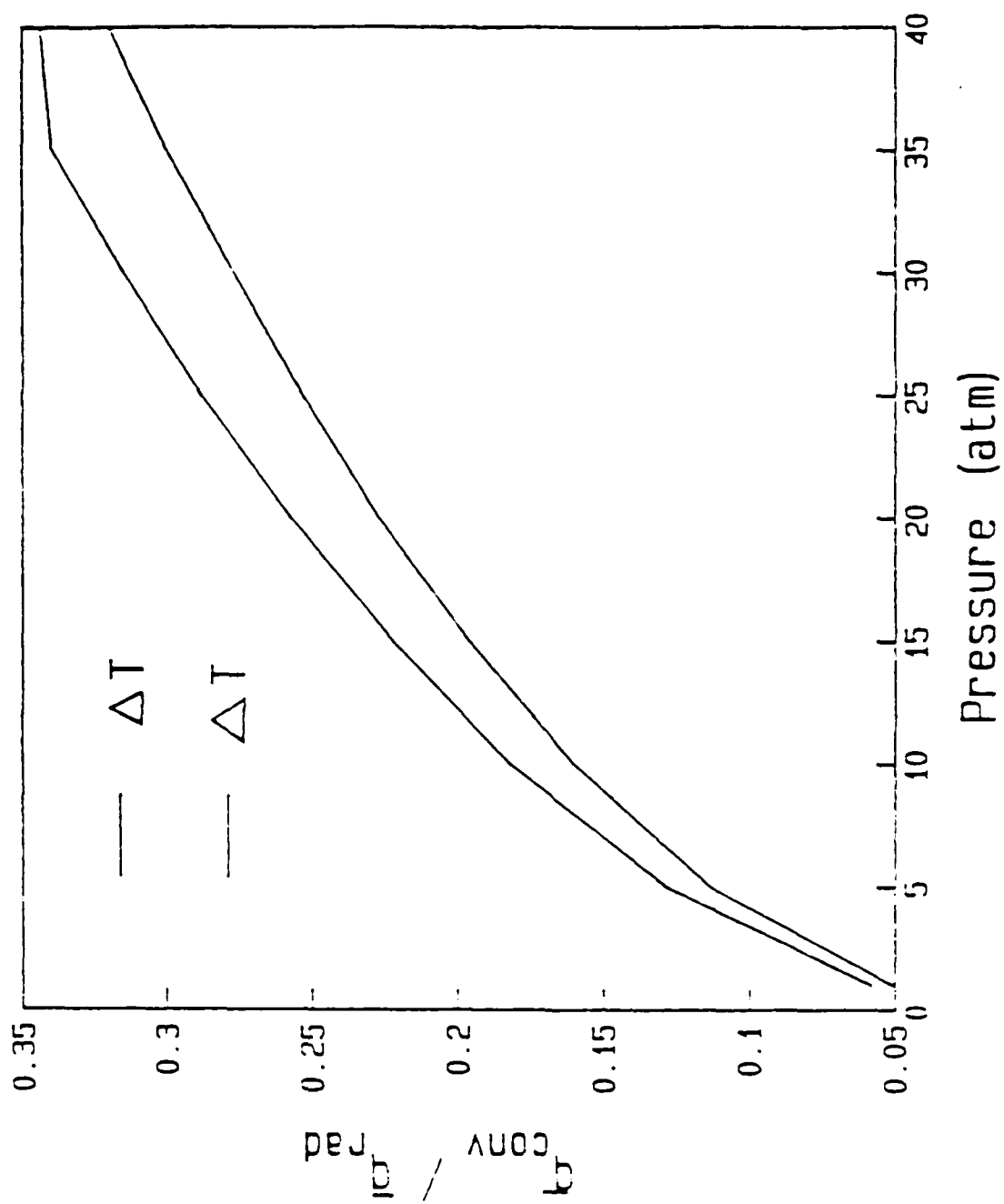
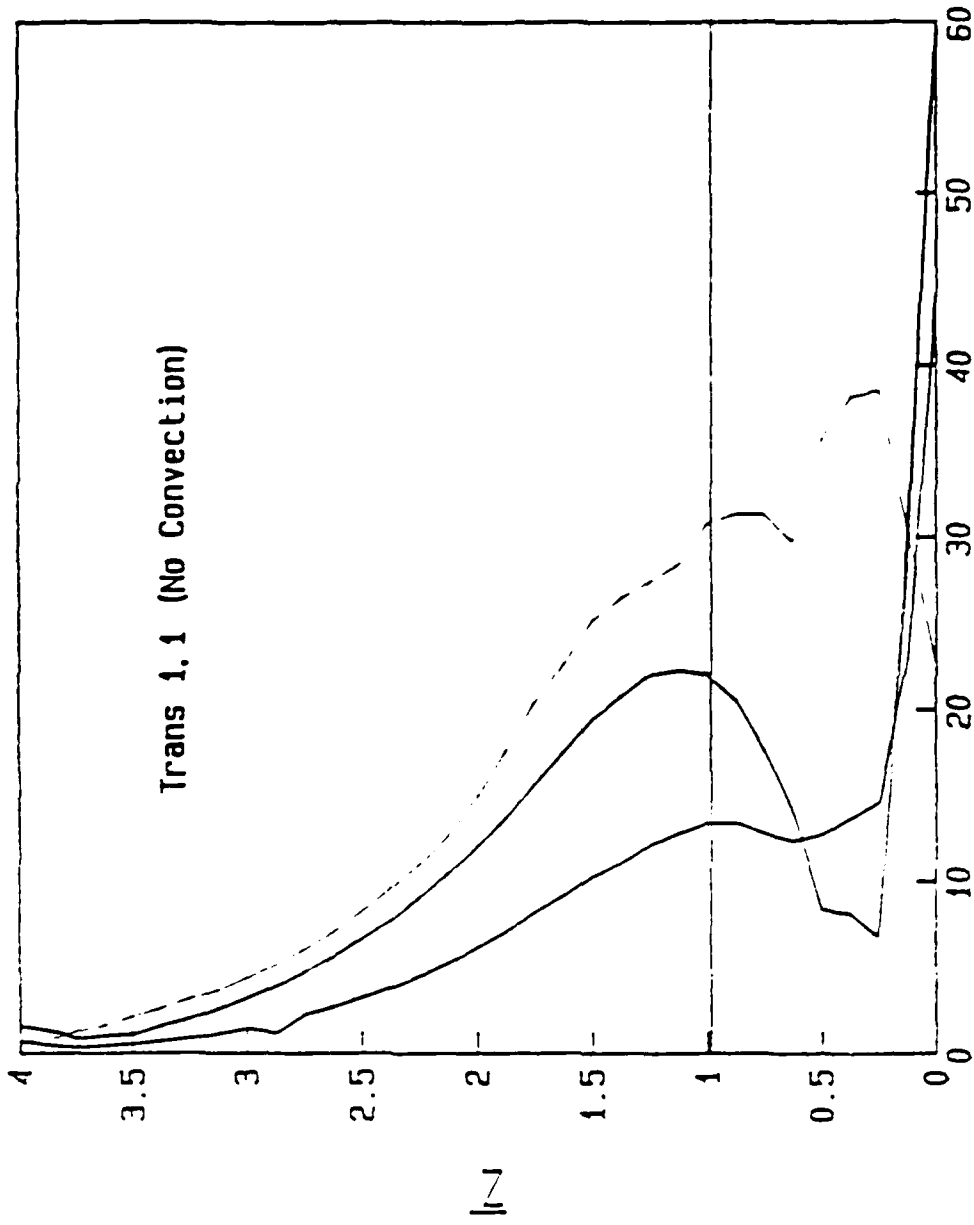
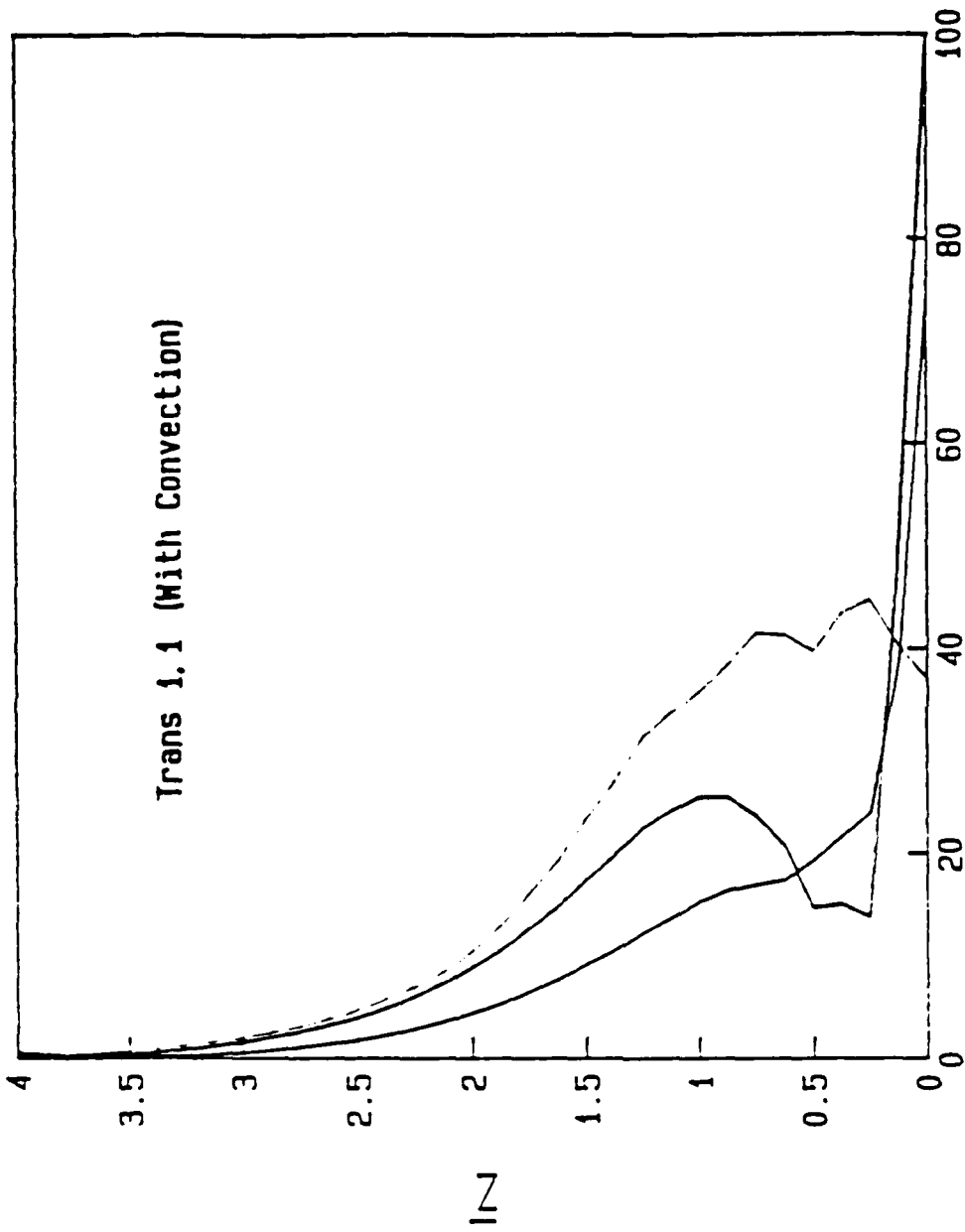


Fig. 11.1



Δ_e

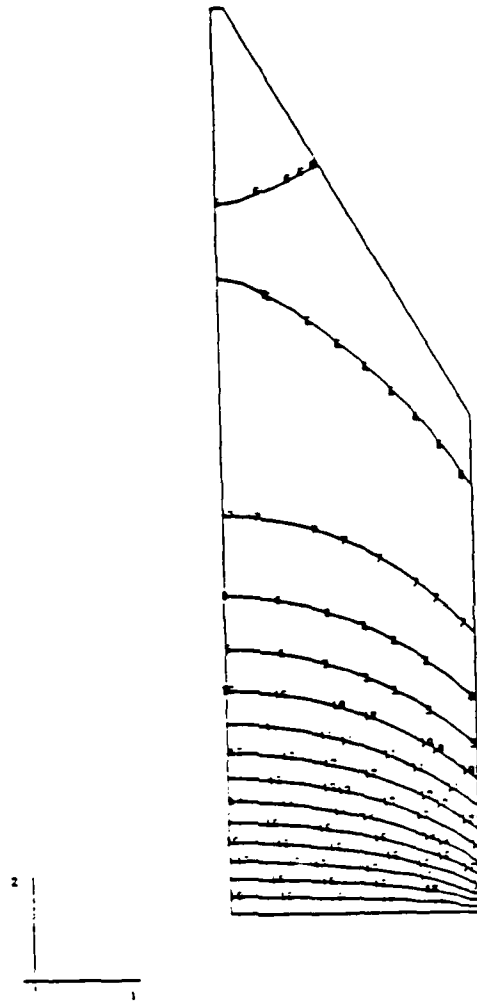
Fig. 11.2



∇_e

Fig. 11.3

TEMP.
 1.0. UNLIE
 1 +7.88E-01
 2 +7.15E-01
 3 +7.21E-01
 4 +7.47E-01
 5 +7.62E-01
 6 +7.78E-01
 7 +7.94E-01
 8 +8.10E-01
 9 +8.26E-01
 10 +8.42E-01
 11 +8.57E-01
 12 +8.73E-01
 13 +8.89E-01
 14 +9.05E-01
 15 +9.21E-01
 16 +9.36E-01
 17 +9.52E-01
 18 +9.68E-01
 19 +9.84E-01
 20 +1.00E+00

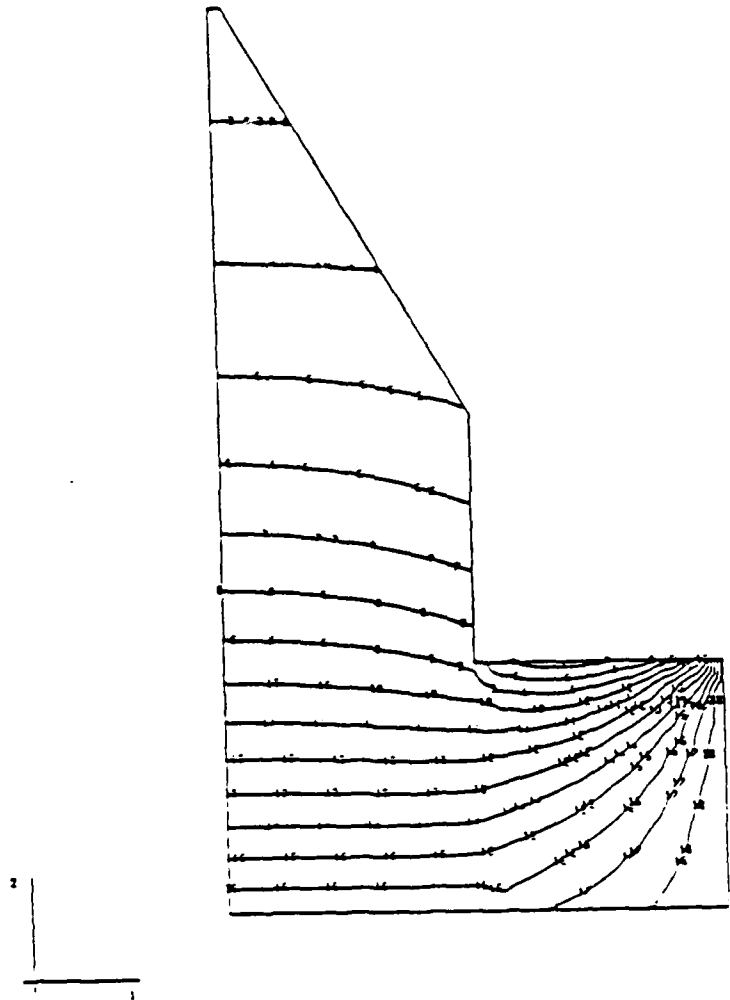


CONE 1, ISOTHERMS, $L_0/r = 2$

STEP 1 (HORIZONTAL) SINGLE (VERTICAL) 4-4-171

FIG. 11.4

TEMP.
 I.D. M/LAX
 1 =5.88E-01
 2 =5.31E-01
 3 =5.82E-01
 4 =5.94E-01
 5 =4.28E-01
 6 =6.57E-01
 7 =6.87E-01
 8 =7.21E-01
 9 =7.82E-01
 10 =7.84E-01
 11 =8.18E-01
 12 =8.47E-01
 13 =8.78E-01
 14 =9.18E-01
 15 =9.42E-01
 16 =9.72E-01
 17 =1.00E+00
 18 =1.02E+00
 19 =1.00E+00
 20 =1.18E+00



CONE1, ISOTHERMS, $L_0/r=2$

STEP 1, ICHORD=1 ANGLE VERSION 4-4-171

Fig. 22-5

Shoulder of Crystal Still in
Opaque Encapsulant

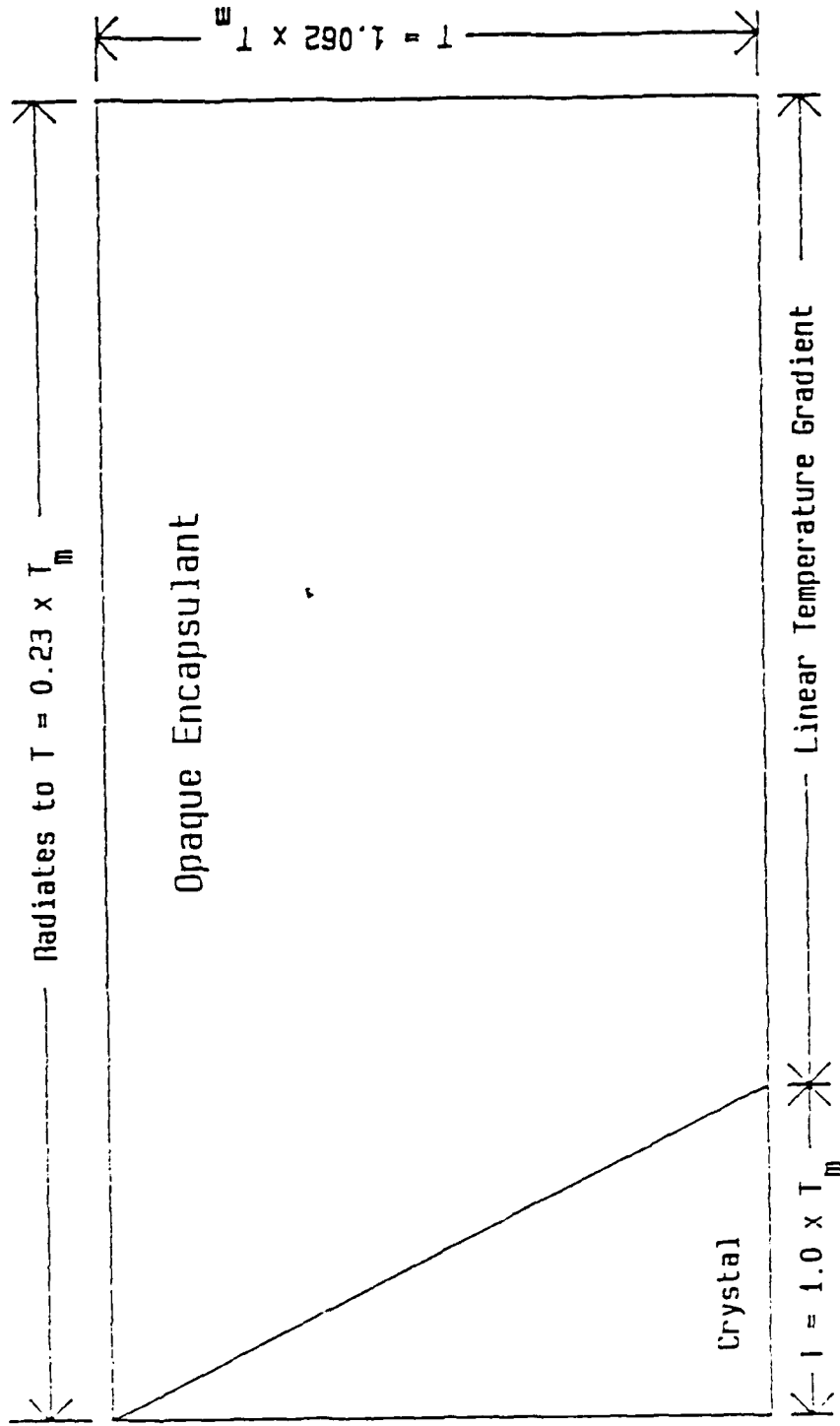


Fig. II.6

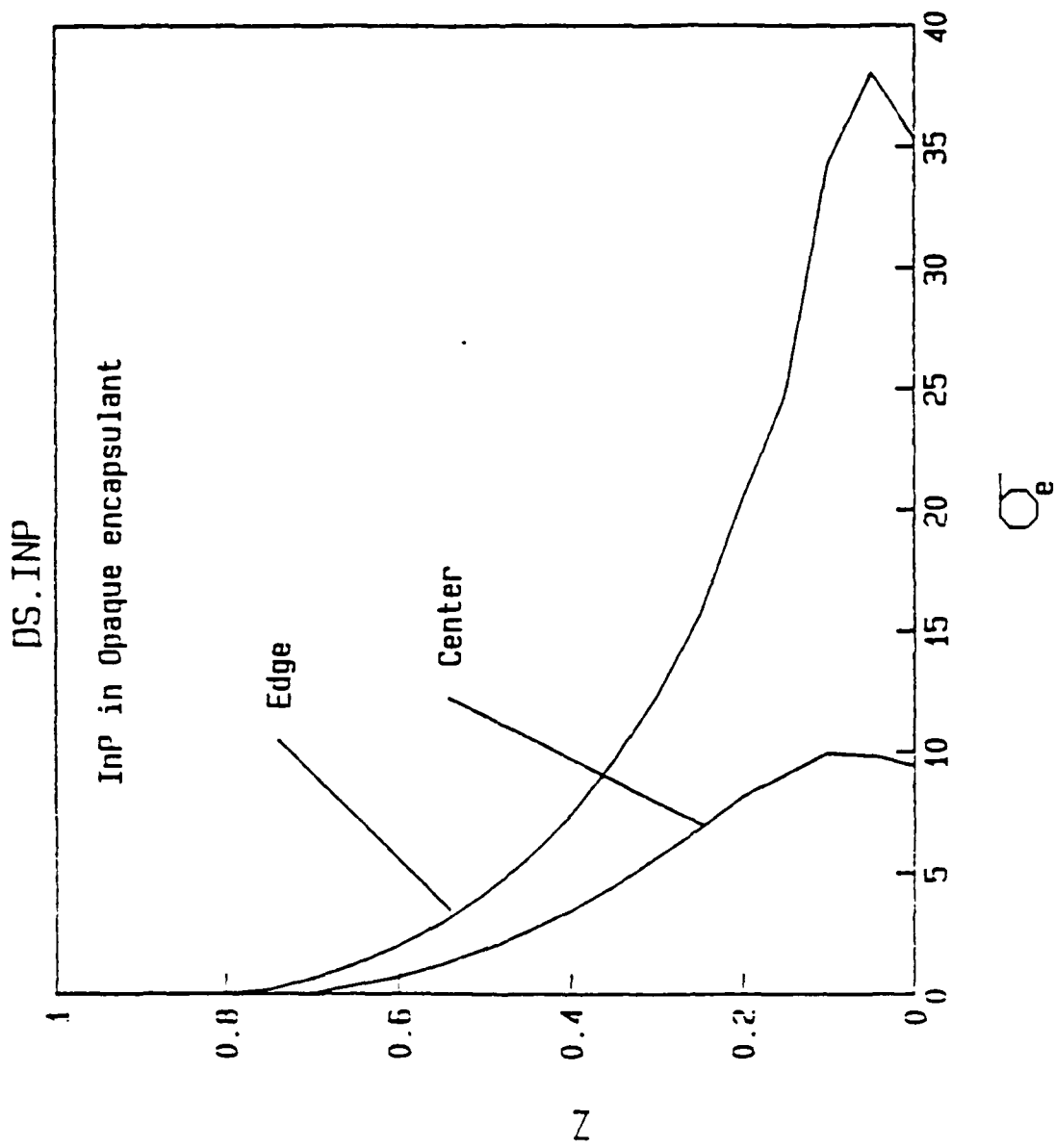
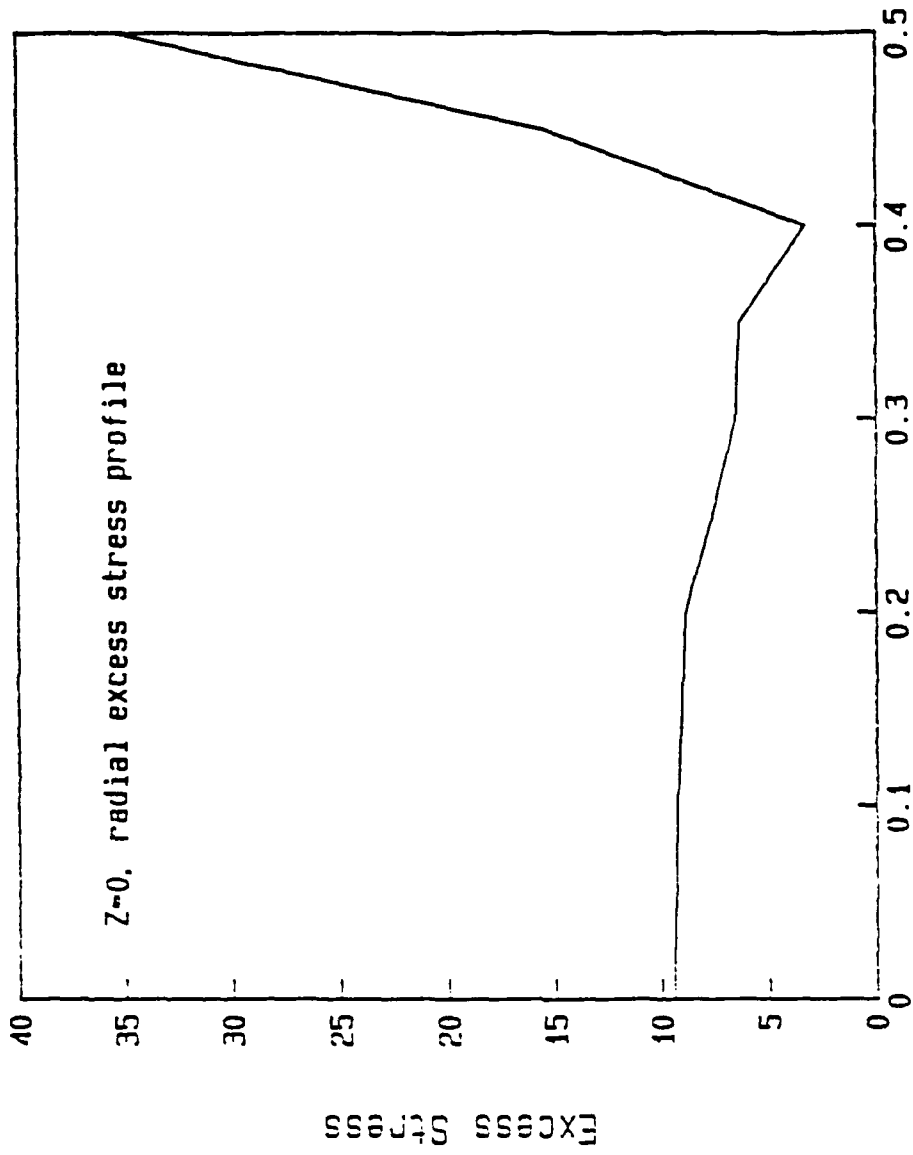


Fig. 11.7

DS.INP



R

Fig. 11.8

DS. INP

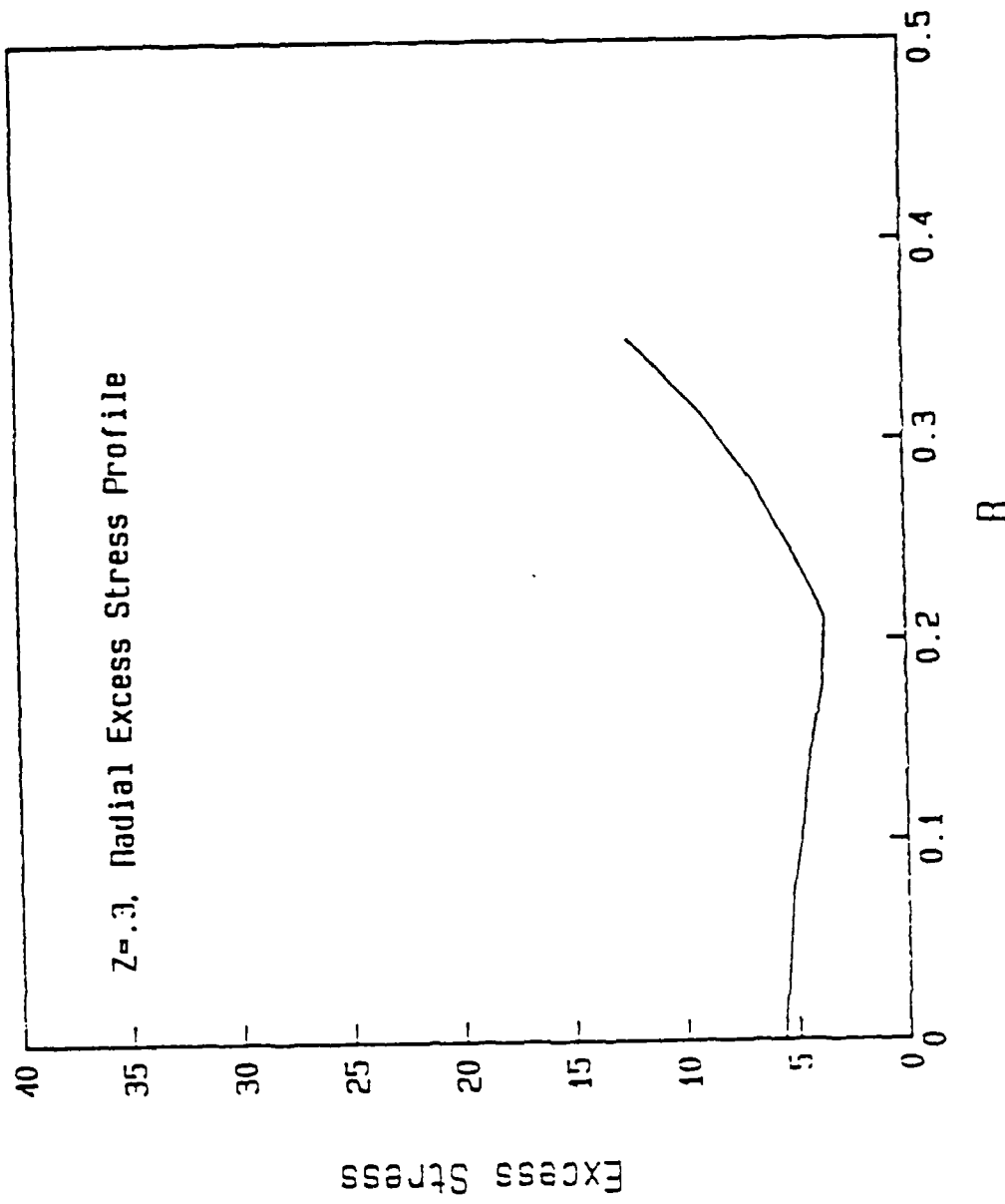


Fig. 11.9

DS. INP

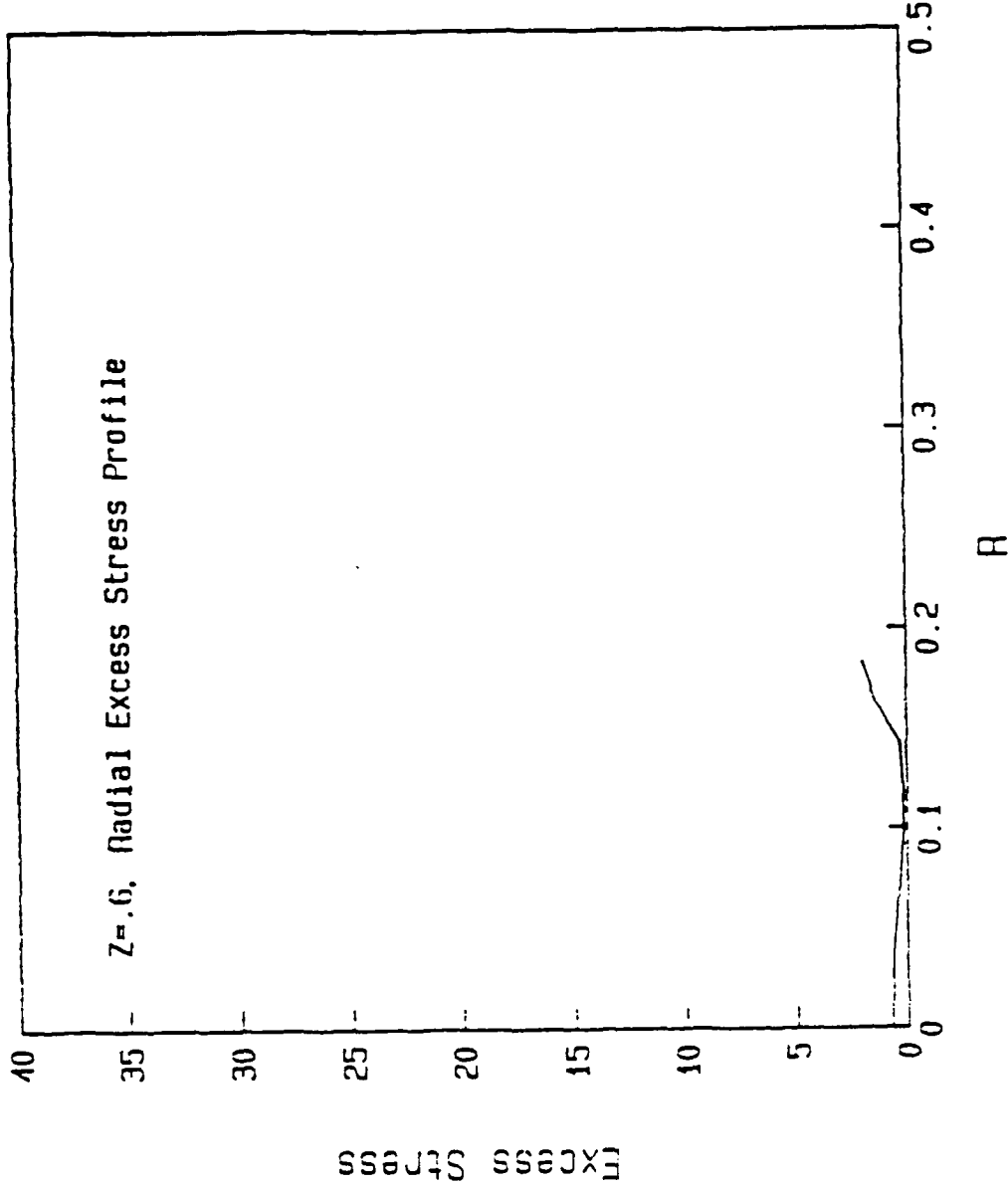


Fig. 11.10

DS. INP

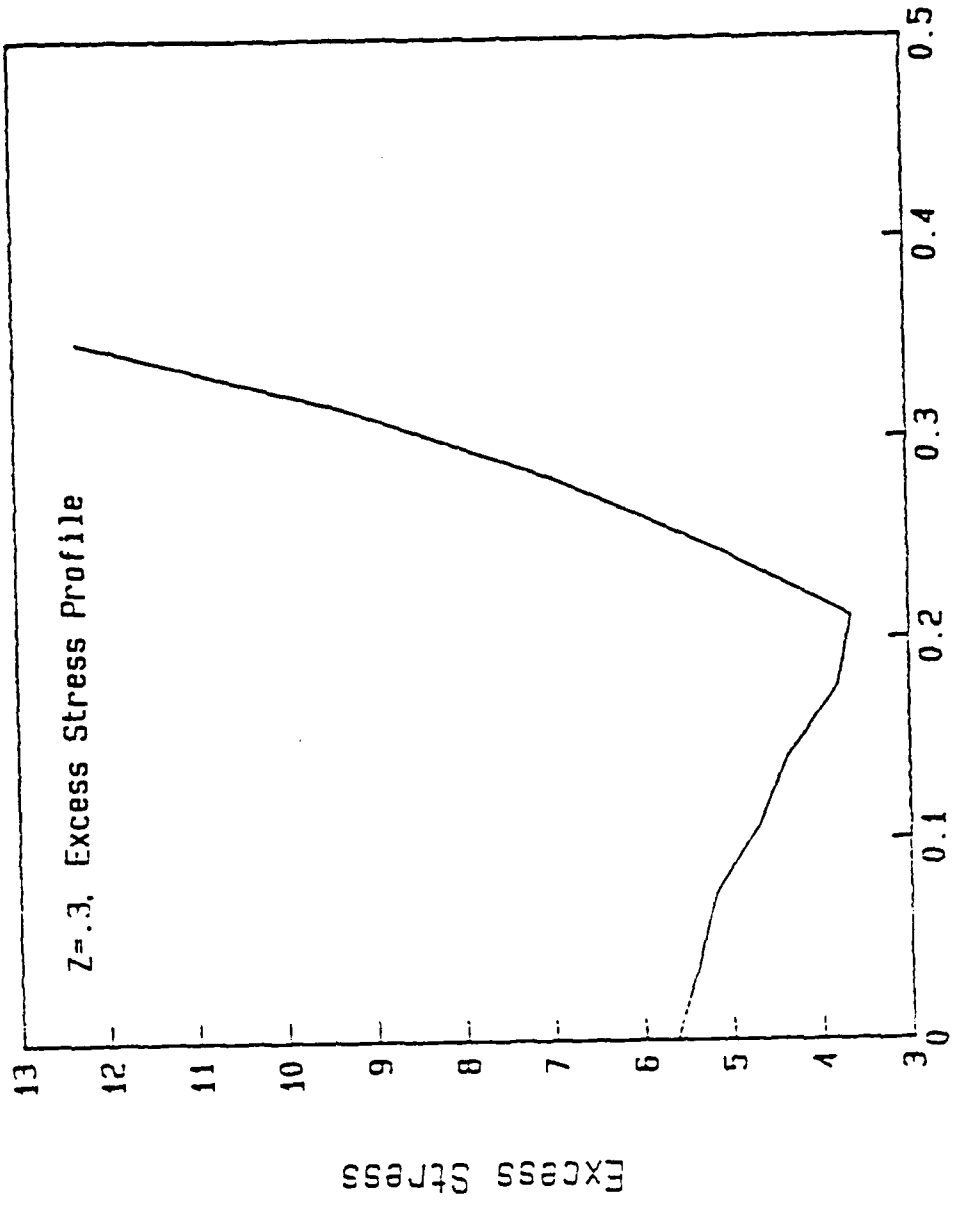


Fig. 11.11

DS. INP

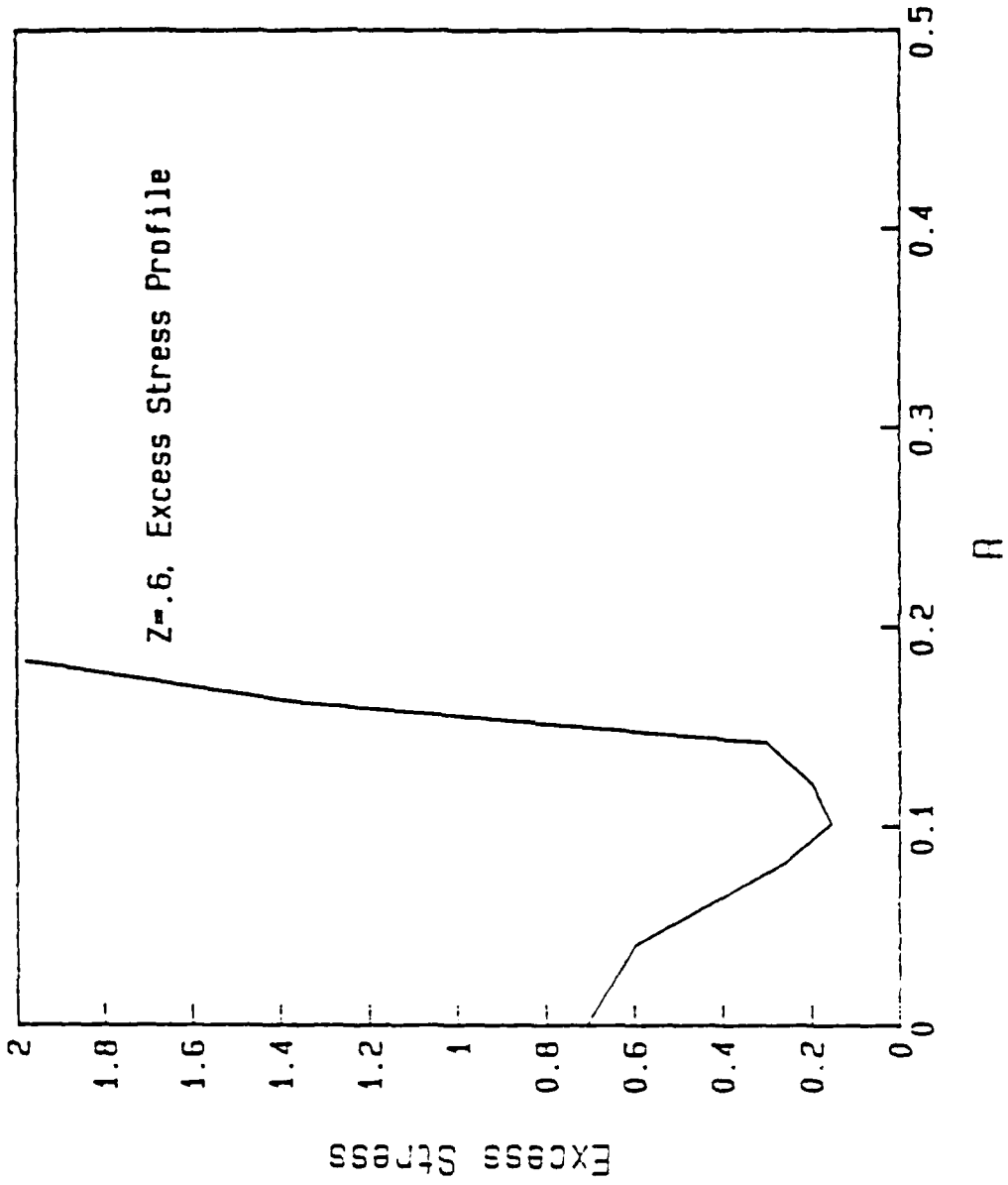


Fig. II.12

Crystal Shoulder Emerging from Opaque Encapsulant

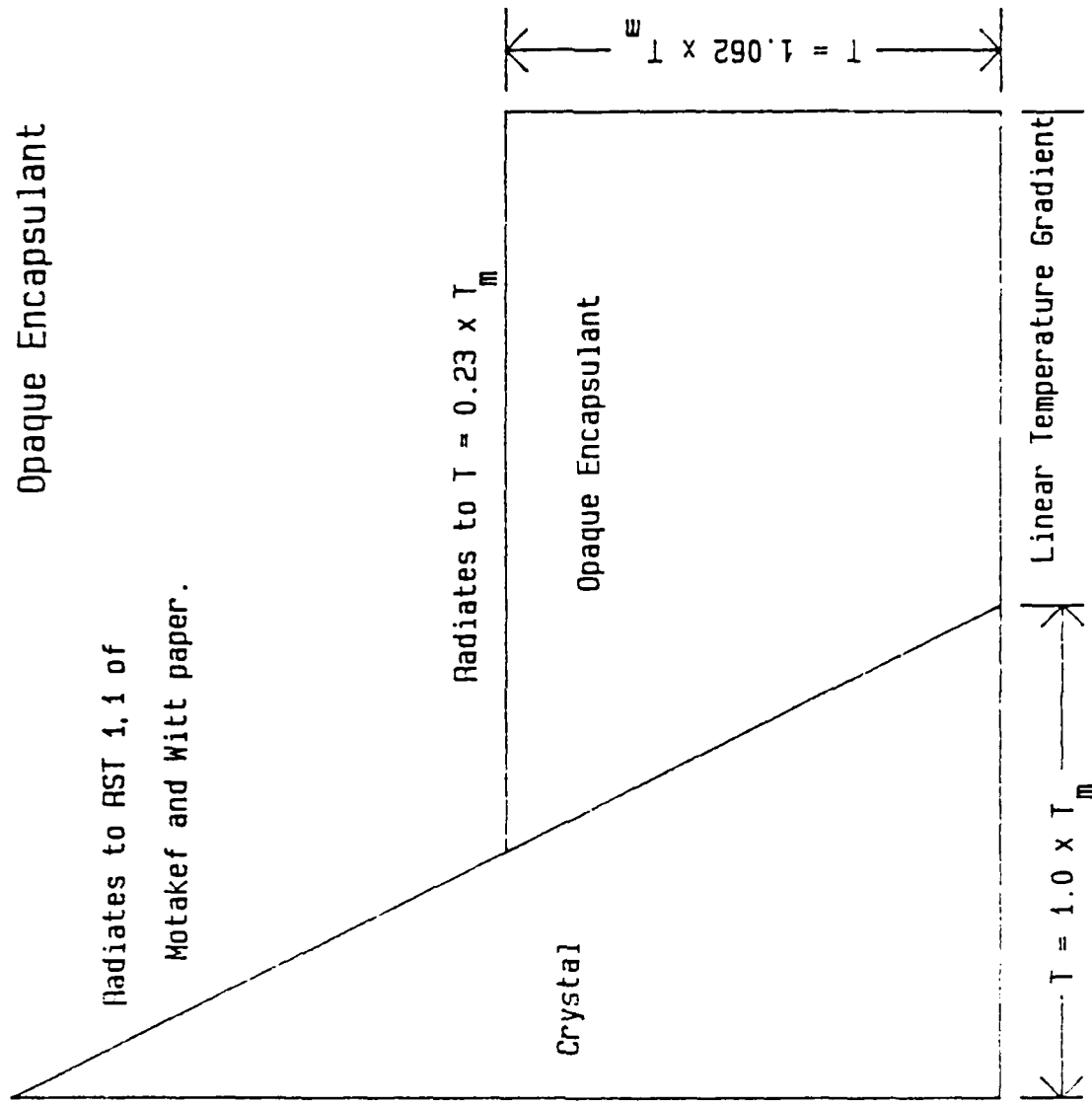


Fig. II.13

DSE.INP

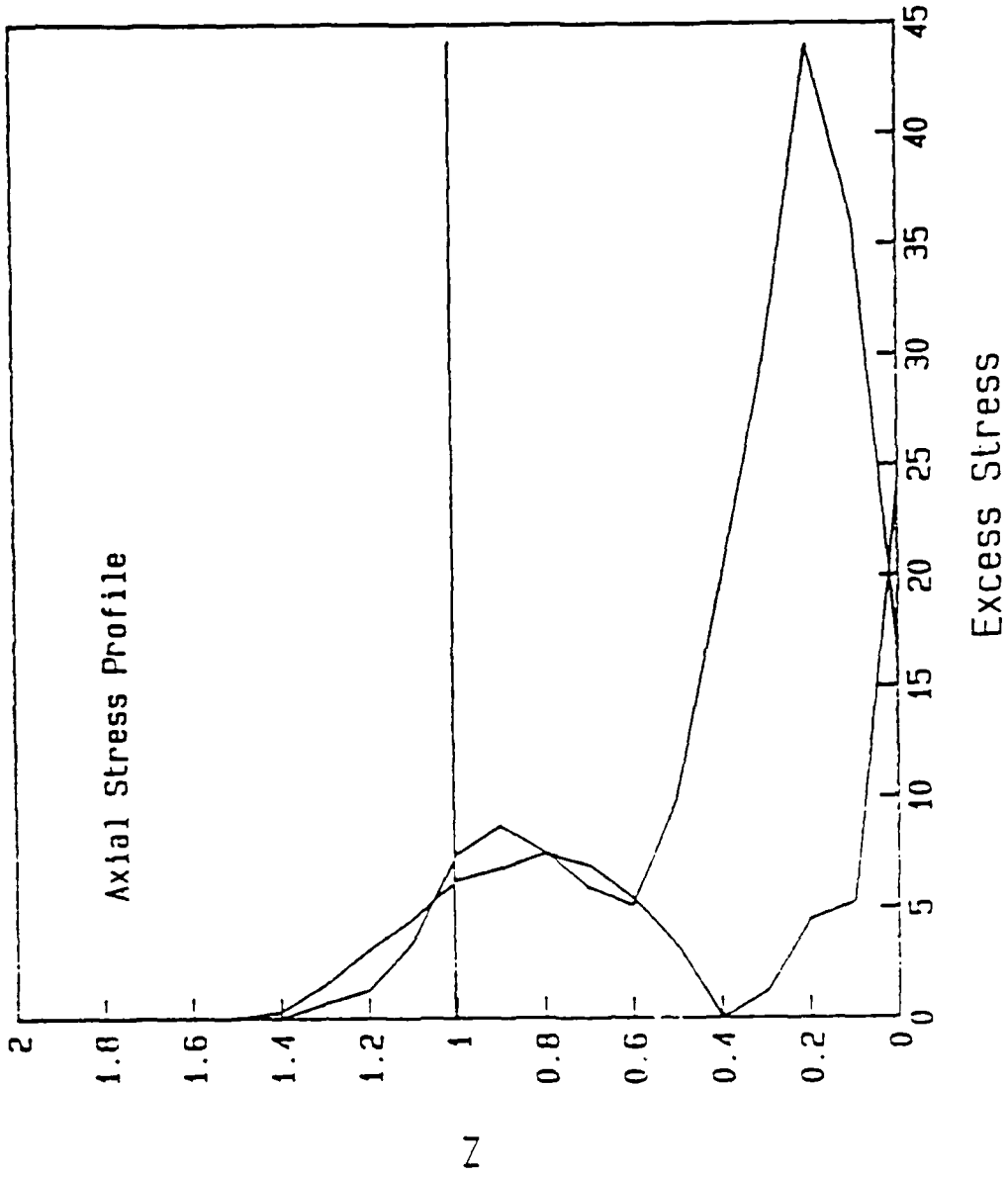


Fig. II.14

DSE.INP

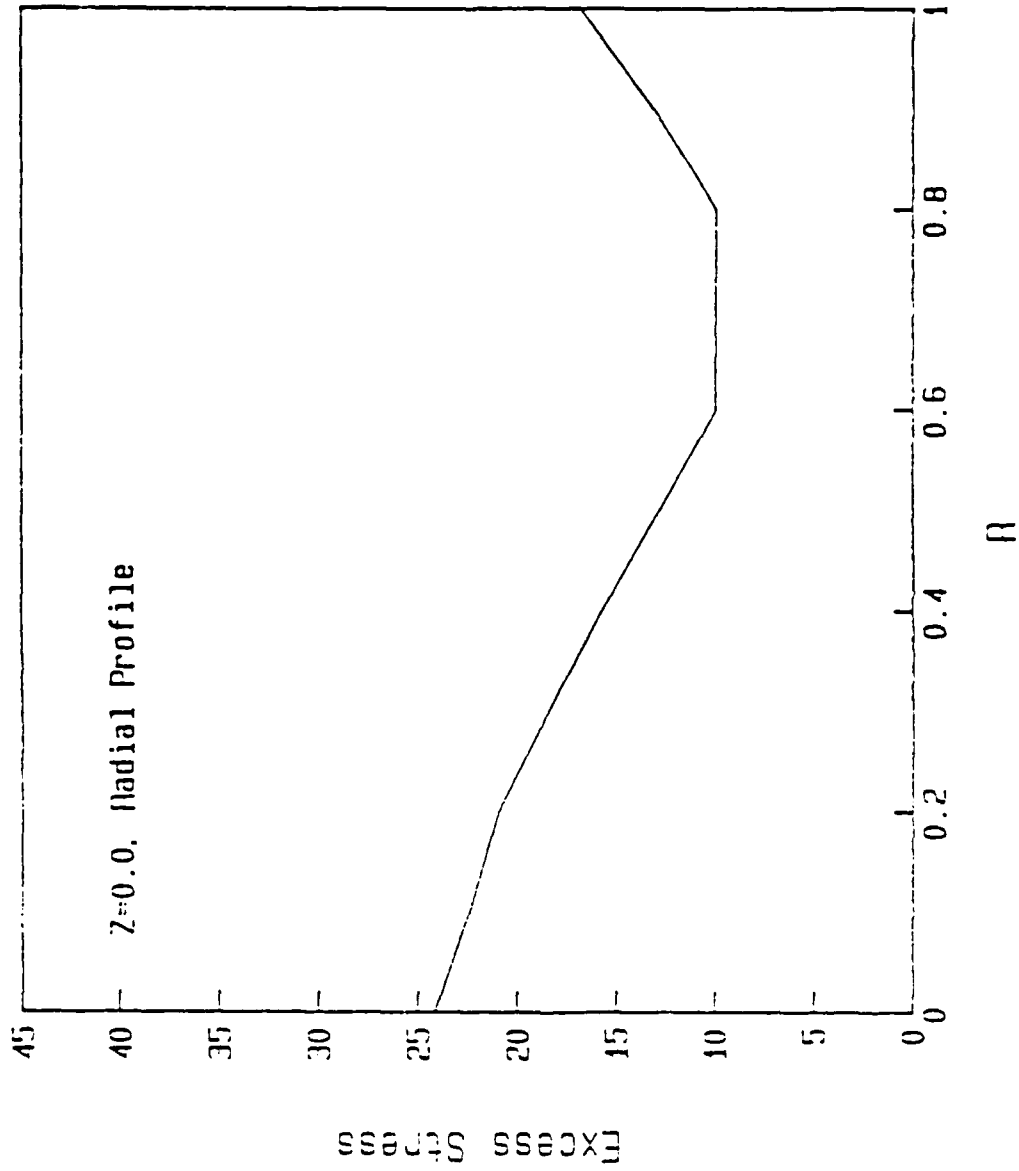
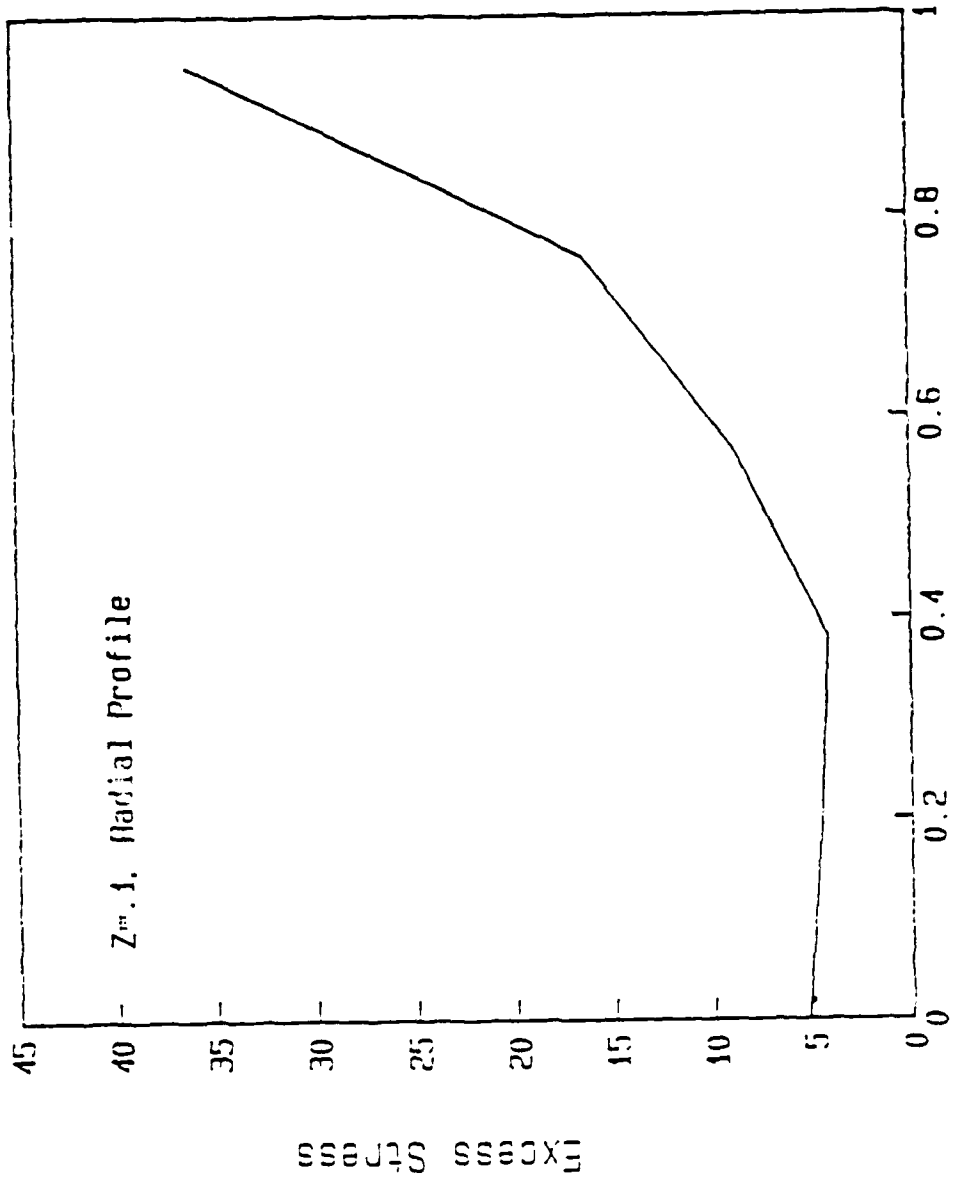


Fig. 11.15

DSE.INP



r

Fig. 11.16

DSE.INP

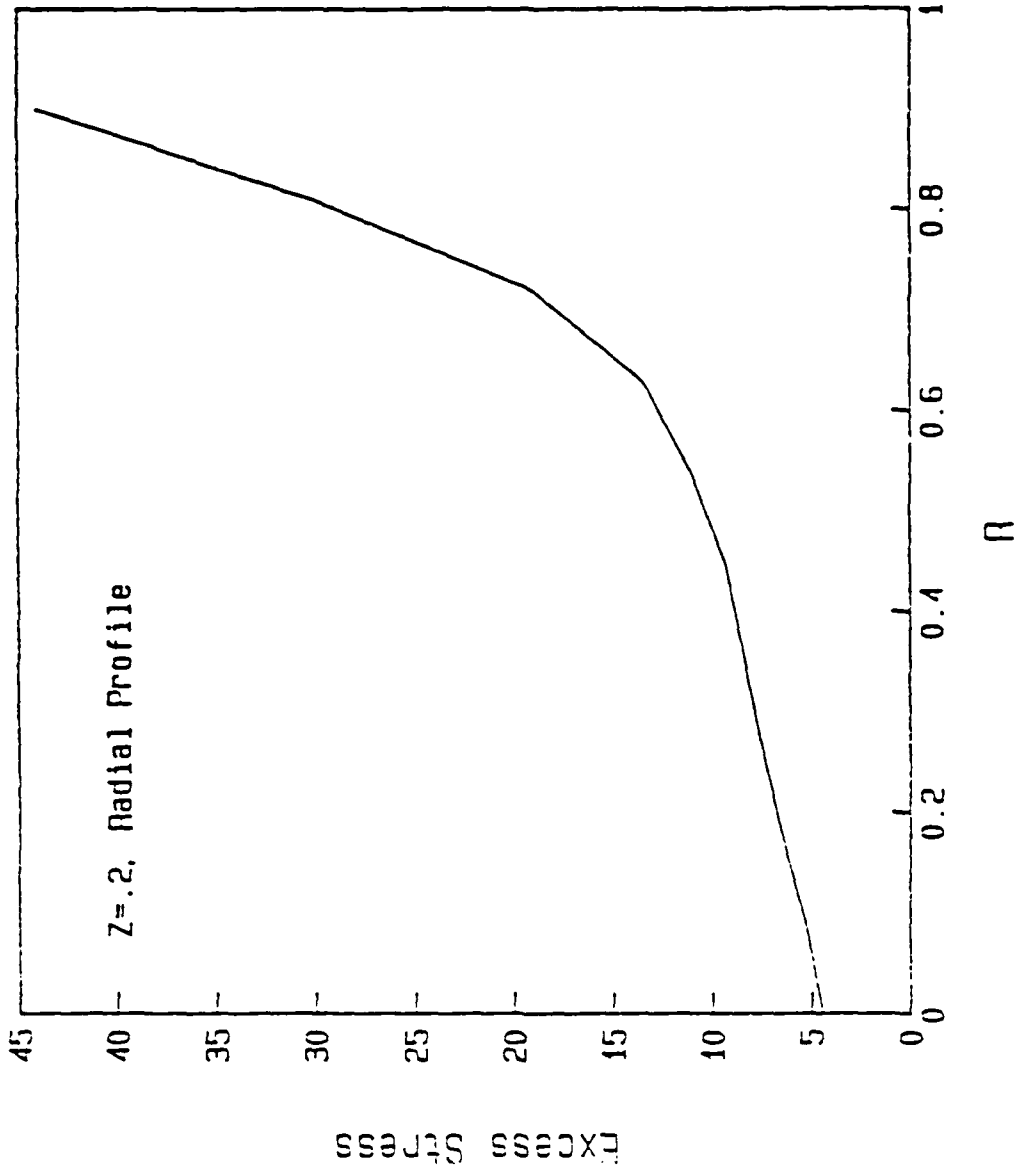


Fig. 11.17

DSE.INP

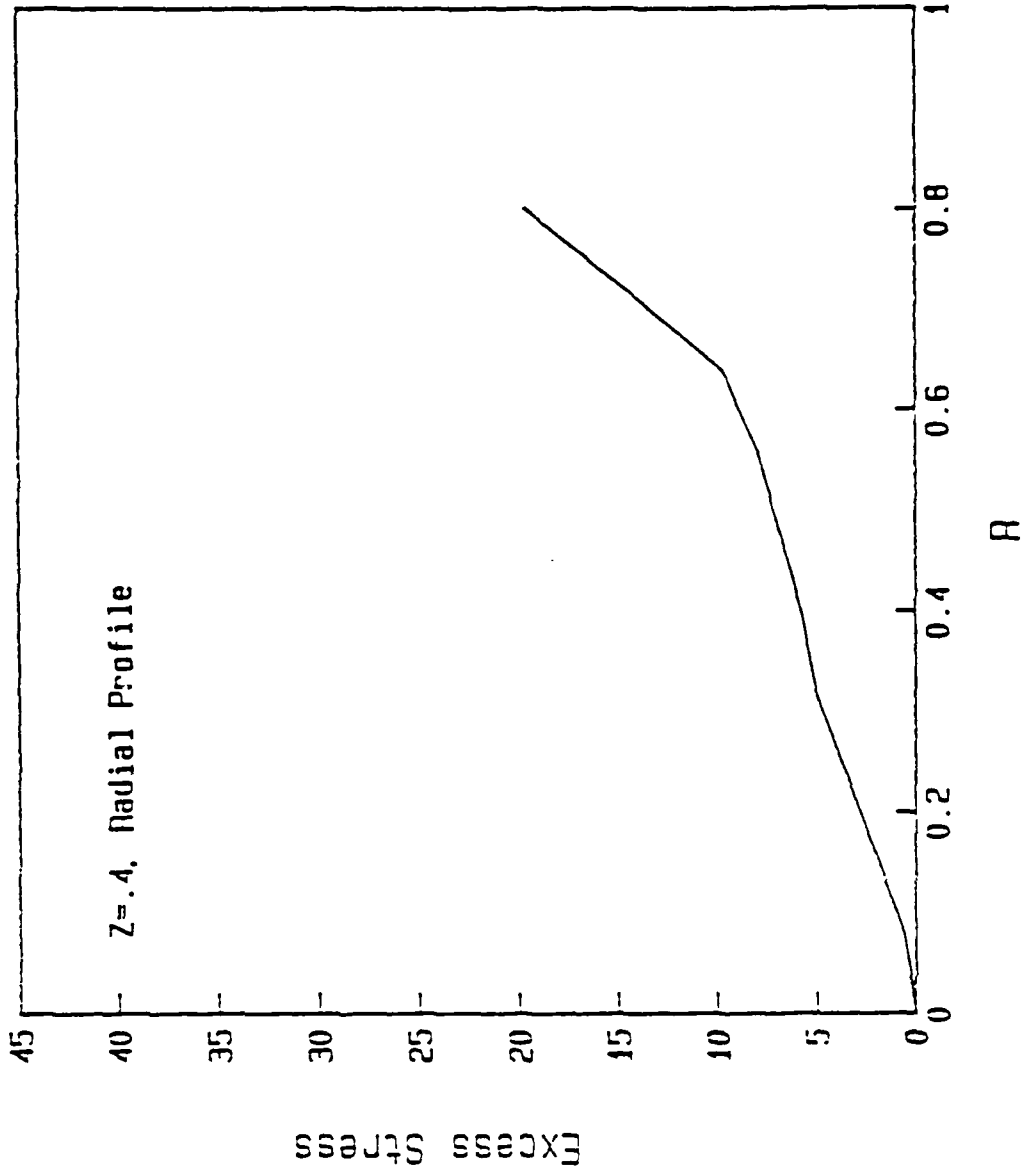


Fig. 11.18

DSE.INP

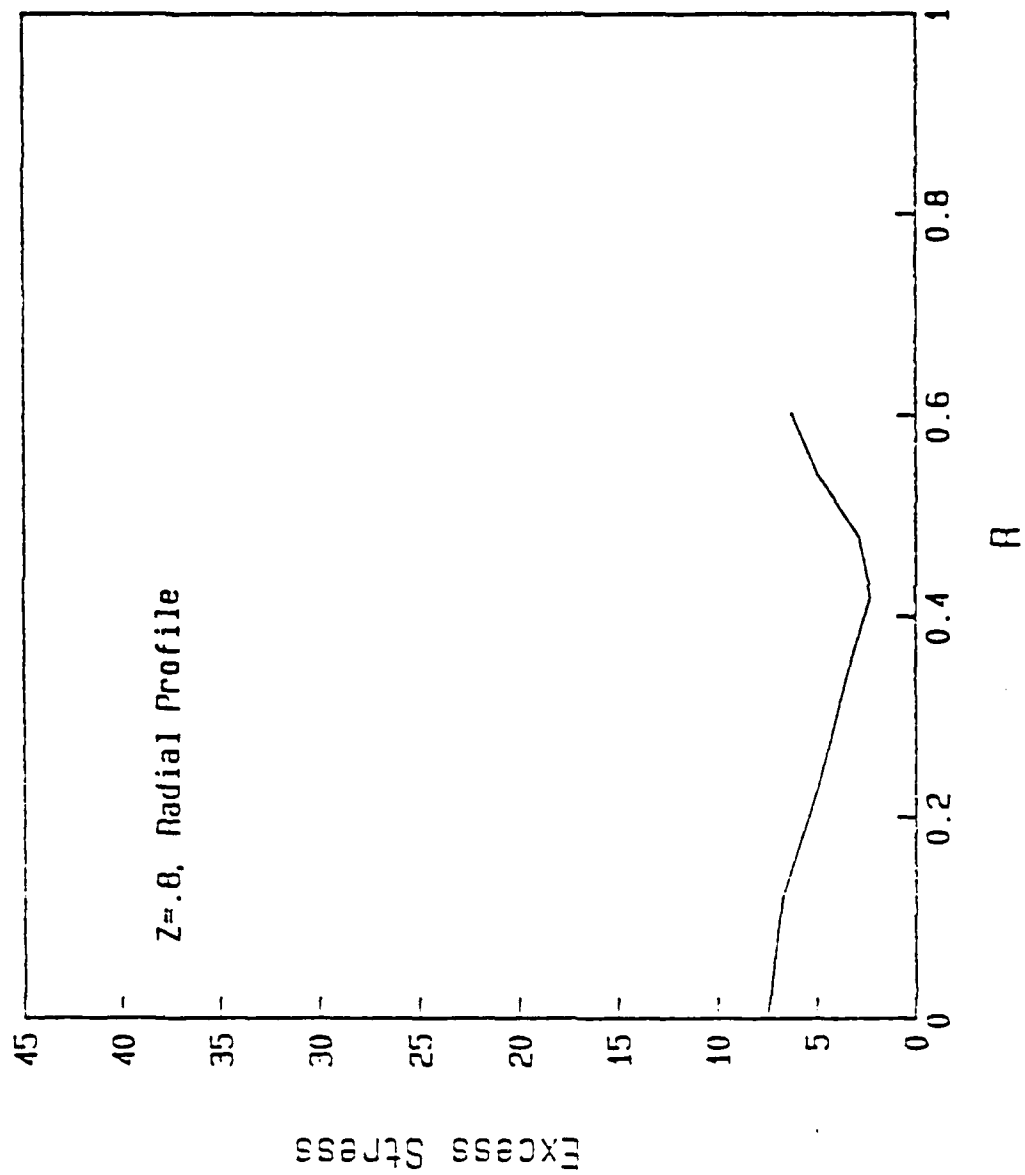


Fig. 11.20

DSE.INP

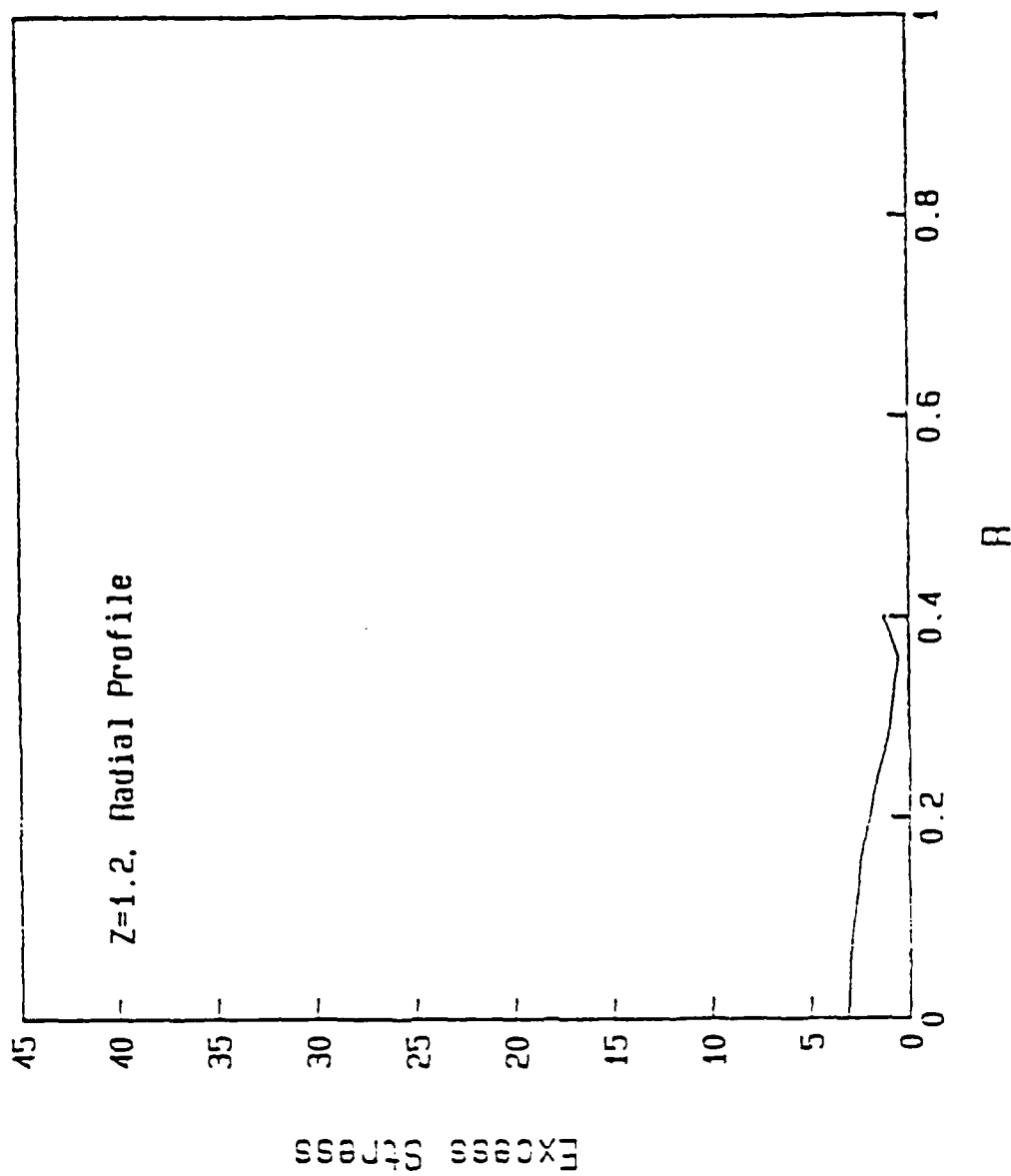


Fig. 11.21

III. NIR Microscopy of N-type III-V Compound Semiconductors

Compositional inhomogeneities have a major effect upon the electrical and optical properties of semiconductor materials. Techniques which permit the qualitative and quantitative characterization of these variations (on a microscale) in III-V semiconductors are virtually non-existent. Near infrared microscopy provides a technique which shows the potential of filling this need.

Free Carrier Absorption

N-type GaAs and InP exhibit free carrier absorption in the infrared. This absorption phenomenon holds a potential for compositional characterization of these materials. Free carrier absorption is a non-direct process involving the scattering of electrons in the conduction band. In examining the potential of this effect for materials characterization, the theoretical calculations of Walukiewicz et al. [1,2] are used as a basis.

In modelling free carrier absorption in GaAs and InP Walukiewicz considered the effect of acoustical phonon scattering, optical phonon scattering, and ionized impurity scattering upon the absorption coefficient. The total absorption due to free carriers thus becomes:

$$\alpha_t(\lambda) = \alpha_{op}(\lambda) + \alpha_{ac}(\lambda) + \alpha_{imp}(\lambda)$$

where:

$$\alpha_{op, \lambda_1} = \alpha_{op, \lambda_0} \left(\frac{\lambda_1}{\lambda_0} \right)^{2.5}$$

$$\alpha_{ac, \lambda_1} = \alpha_{ac, \lambda_0} \left(\frac{\lambda_1}{\lambda_0} \right)^{1.5}$$

$$\alpha_{imp, \lambda_1} = \alpha_{imp, \lambda_0} \left(\frac{\lambda_1}{\lambda_0} \right)^{3.5}$$

In figures 1 and 3 the theoretical free carrier absorption characteristics of GaAs and InP with electron concentrations of $10^{16}/\text{cm}^3$ and $10^{18}/\text{cm}^3$ are presented. From these curves it can be seen that the absorption coefficient is largest in the mid-IR, with the absorption coefficient of InP rising more rapidly than that of GaAs. In figures 2 and 4, the same data is plotted in the wavelength range of interest to near

infrared microscopy. It can be seen from these two graphs that a moderately doped sample will show very little wavelength dependence of the absorption coefficient. In fact, this doping range would require thick samples for any measurable transmittance change to occur. The transmittance is given by:

$$T = \frac{(1 - R)^2 \exp(-\alpha d)}{1 - R^2 \exp(-2\alpha d)}$$

where:

- R = Reflectance
- T = Transmittance
- d = sample thickness
- α = absorption coefficient

The general validity of these calculations can be seen in fig. 5 where the free carrier absorption of InP:Sn crystal is shown.

For near IR transmission light microscopy to be a viable approach to micro-segregation characterization, the absorption coefficient must show sensitivity to the free electron concentration. Figure 6 shows this dependence for a radiation with a wavelength of 1 μm . In excellent agreement with previously reported absorption measurements on n-type GaAs [3], a nearly linear relationship between the absorption coefficient and the electron concentration is exhibited.

Experimental Conditions for Analysis

NIR characterization requires an optical system consisting of a uniform, stable light source and a sensitive detecting device. Also required is the ability to quantify the transmitted light intensity sensed by the detector. To accomplish this, an Axitron microscope (Zeiss) in combination with a silicon based, extended range infrared TV camera (Dage-MTI) were used. The resulting image was processed utilizing a 512 x 512 x 256 image processing system (Recognition Technology) resident in a super-mini-computer (MassComp). This system allows for the quantification of the light intensity at every pixel position across the field of view. Thus, theoretically the absorption coefficient and electron (dopant) concentration can be determined for any position in a given wafer.

The potential of this approach is shown in fig. 7, in which a near infrared micrograph on a GaAs:Si sample is shown. With calibration this distribution will be translated into a real-time measurement of the dopant distribution.

Fourier Analysis

Utilizing a light intensity distribution, information related to the spatial distribution of inhomogeneities can be obtained. Through Fourier analysis of this distribution, the

harmonic relationships among the various features were calculated. In this analysis, the light intensity is expressed as:

$$I(x) = \frac{1}{2} \sum c_n e^{i\omega_n x}$$

where:

$$c_n = \frac{1}{L} \int I(x) e^{-i\omega_n x} dx$$

$$\omega_n = \frac{\pi n}{L}$$

where L is the fundamental period of the function and $C_n(\omega_n)$ is the "Fourier spectrum" of the function $I(x)$. In fig. 8 a near infrared micrograph of an InP:Sn crystal is shown with a super-imposed light intensity distribution and Fourier spectrum. In this material the effects of turbulent melt convection are reflected in the random nature of the observed striae as well as in the resulting Fourier spectrum which shows numerous modes indicating the non-periodic nature of the dopant distribution.

References

1. W. Walukiewicz, J. Lagowski, L. Jastrzebski, P. Rava, M. Lichtensteiger, C.H. Gatos, and H.C. Gatos, *J. Appl. Phys.* **51**(2) 2659 (1980).
2. W. Walukiewicz, J. Lagowski, L. Jastrzebski, P. Rava, M. Lichtensteiger, C.H. Gatos, and H.C. Gatos, *J. Appl. Phys.* **50**(2) 899 (1980).
3. W. Spitzer and J. Whelan, *Phys. Rev* **114**(1) 59 (1959).

Theoretical Free Carrier Absorption
In GaAs and InP

$$n \approx 1.0 \times 10^{16} \text{ cm}^{-3}$$

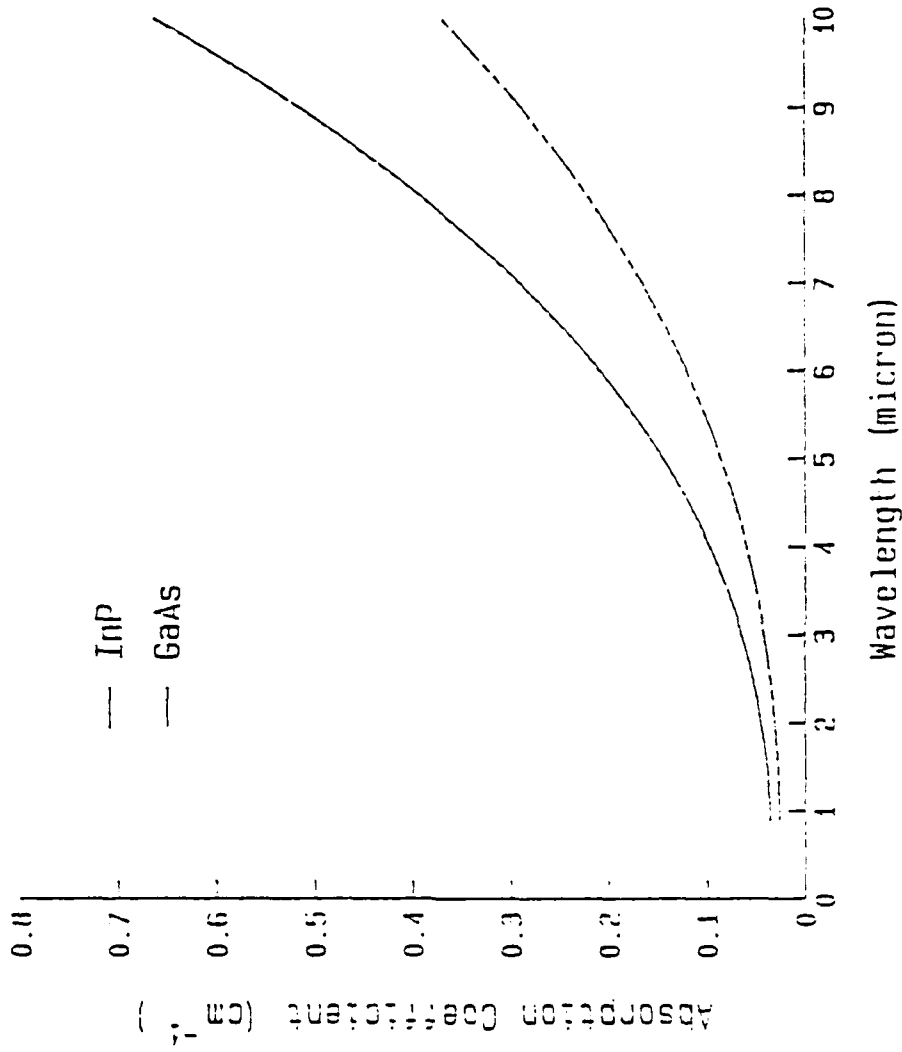


Fig. III.1

Theoretical Free Carrier Absorption

In GaAs and InP

$$n \approx 1.0 \times 10^{16} \text{ cm}^{-3}$$

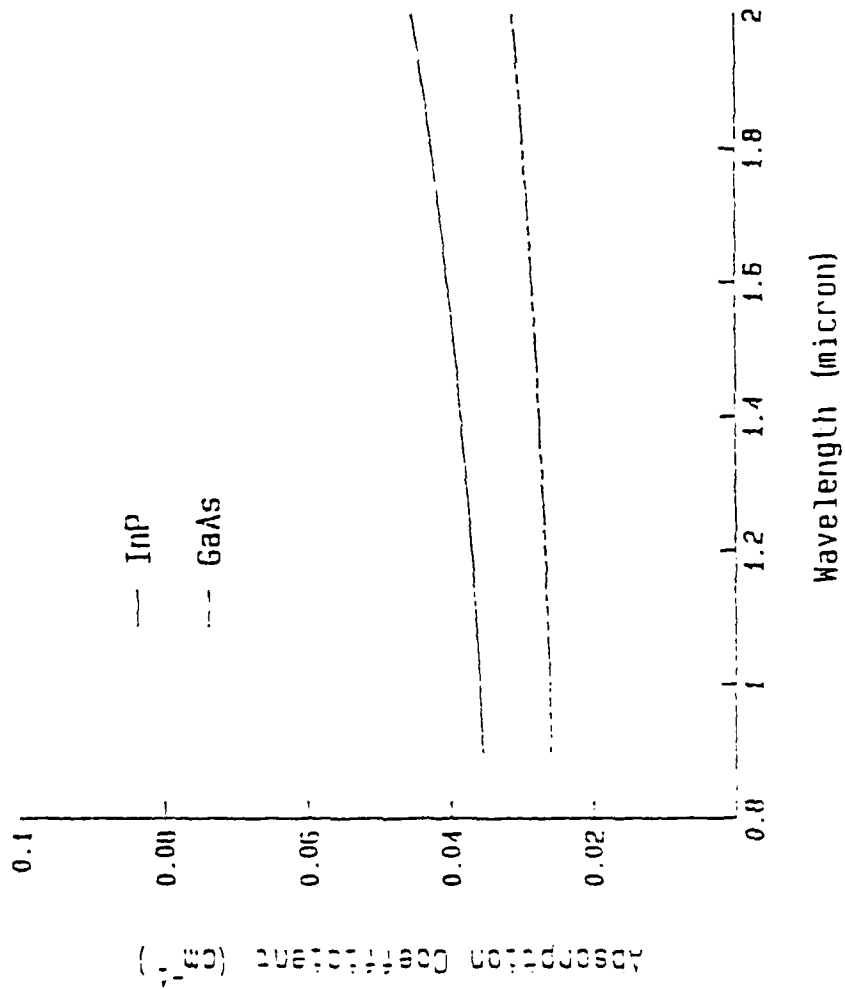


Fig. III.2

Theoretical Free Carrier Absorption

In GaAs and InP

$$n \approx 1.0 \times 10^{18} \text{ cm}^{-3}$$

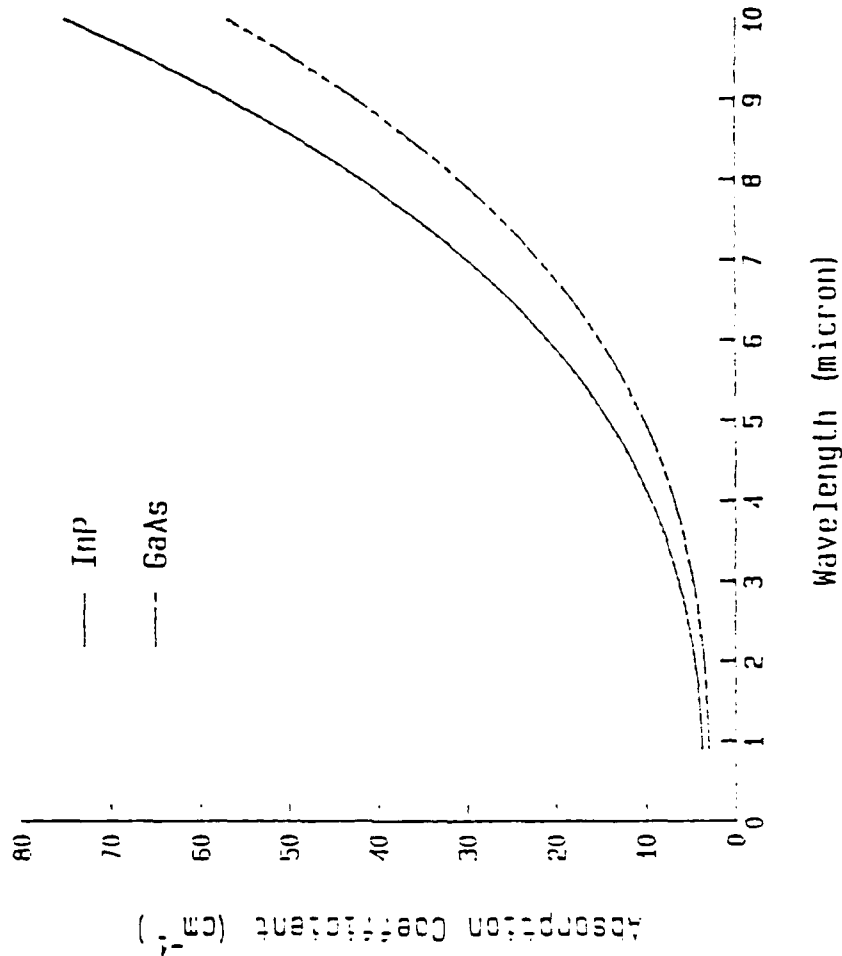


Fig. III.3

Theoretical Free Carrier Absorption

In GaAs and InP

$$n \approx 1.0 \times 10^{18} \text{ cm}^{-3}$$

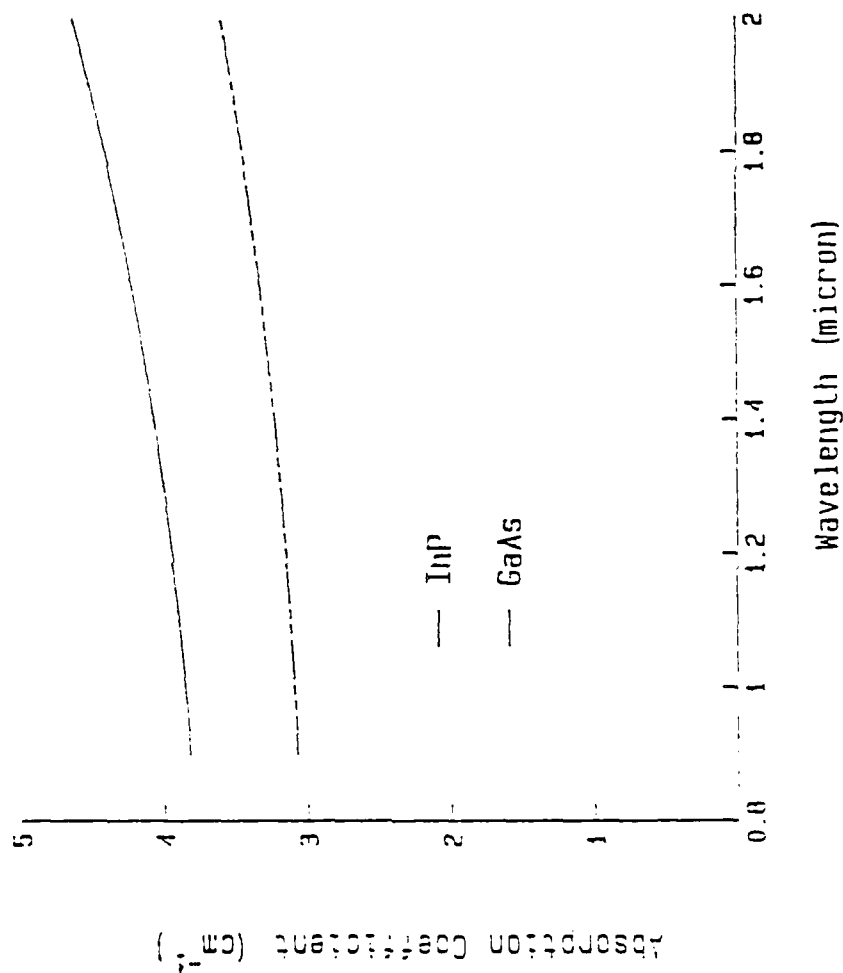


Fig. 111.4

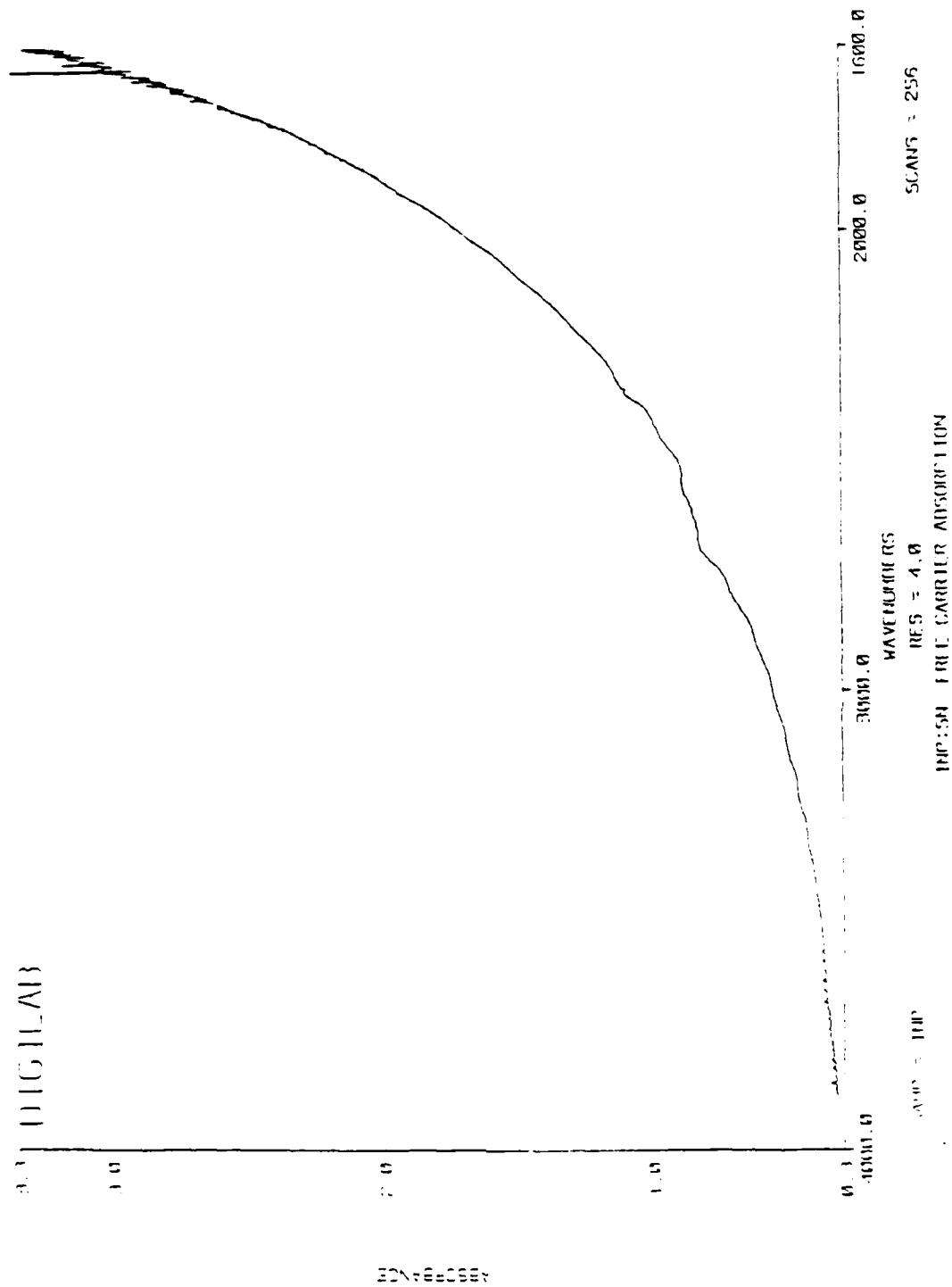


Fig. III.5

Theoretical Free Carrier Absorption
As a Function of Electron Concentration

At 1 Micron
For GaAs and InP

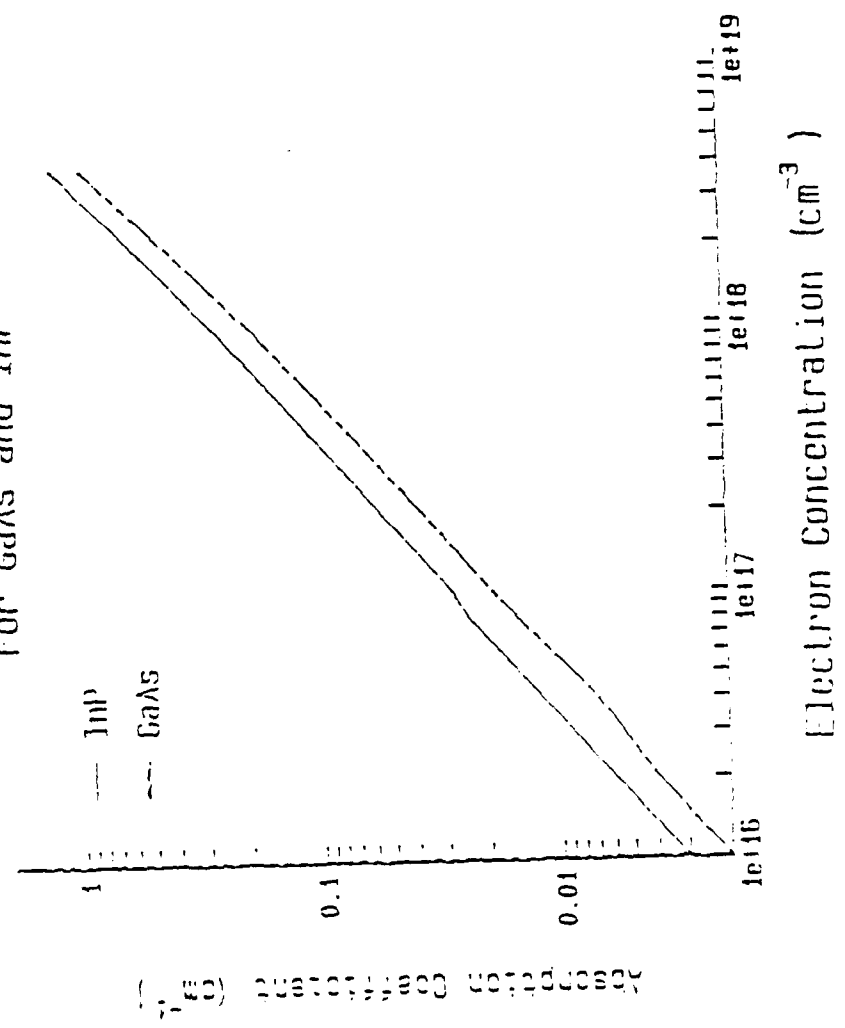


Fig. III.6

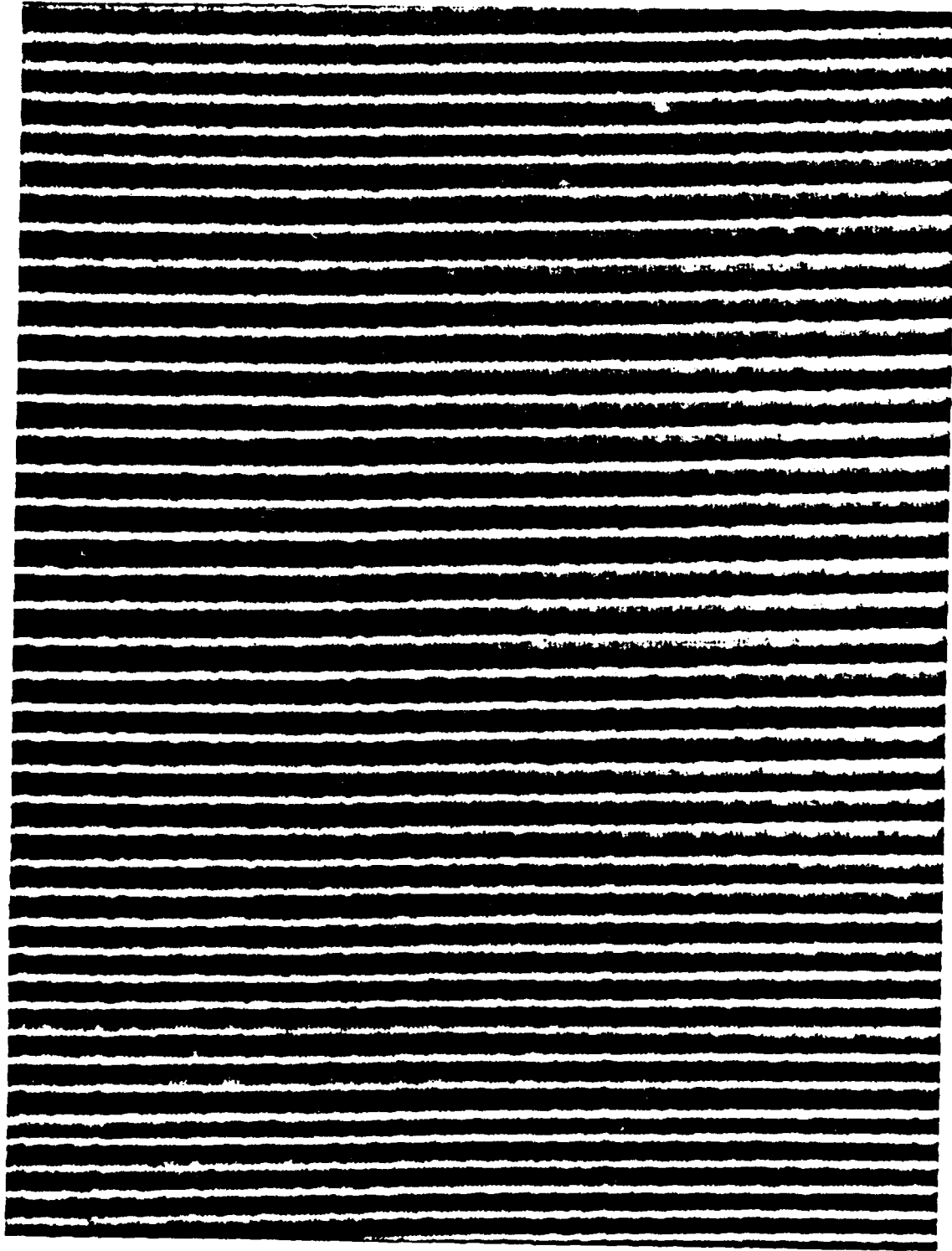


Fig. III.7

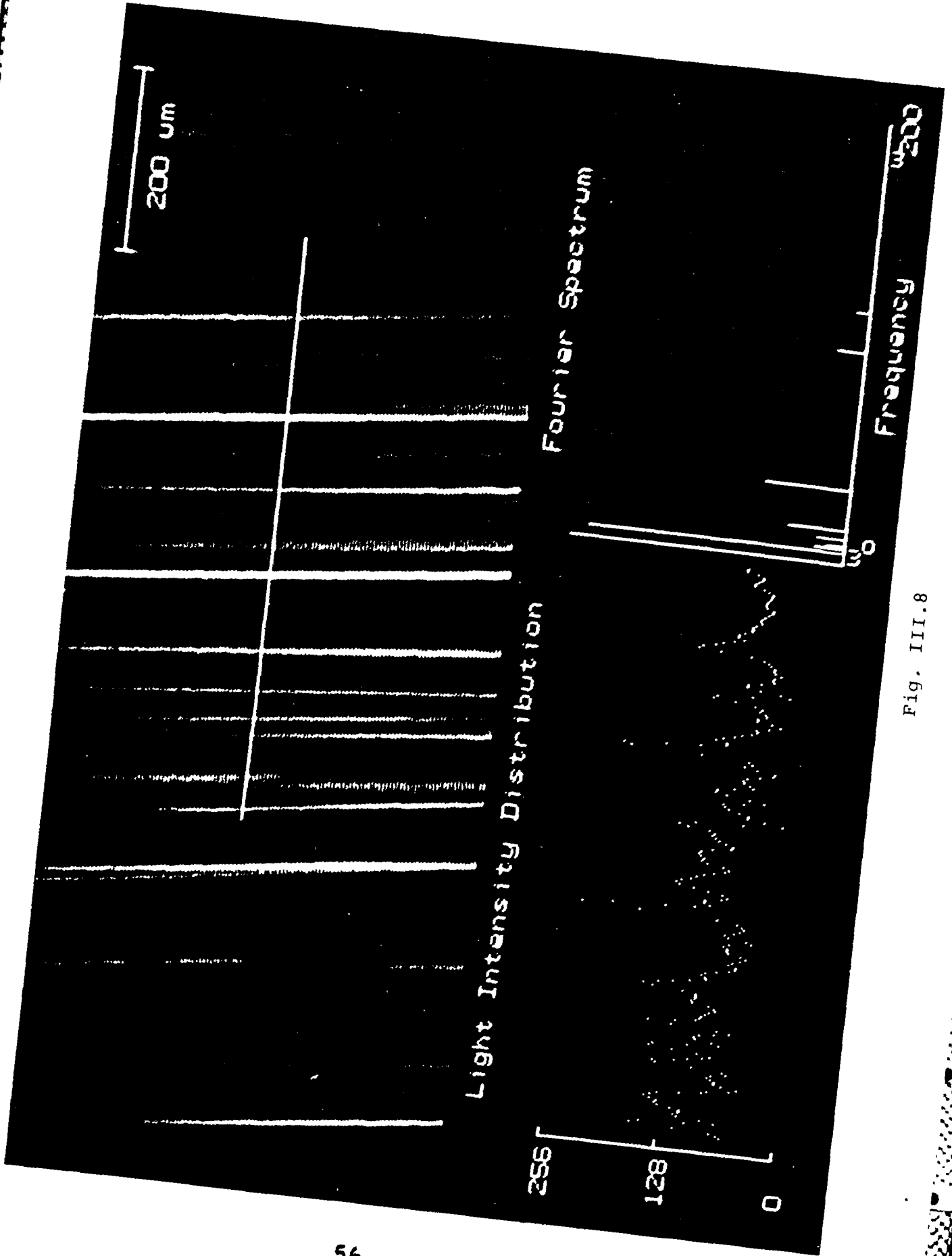


Fig. III.8